Naval Research Laboratory
Stennis Space Center, MS 39529-5004

NRL/FR/7323--97-9673

Validation Test Report for OCEANS 1.0: The 1/4° Global, Reduced Gravity NRL Layered Ocean Model

E. Joseph Metzger
Robert C. Rhodes
Dong Shan Ko
Harley E. Hurlburt

Ocean Dynamics and Prediction Branch
Oceanography Division

June 30, 1998

REPORT DOCUMENTATION PAGE

Form Approved
OBM No. 0704-0188

1. AGENCY USE ONLY *(Leave blank)*	2. REPORT DATE	3. REPORT TYPE AND DATES COVERED
	June 30, 1998	Final

4. TITLE AND SUBTITLE

Validation Test Report for OCEANS 1.0: The 1/4° Global, Reduced Gravity NRL Layered Ocean Model

5. FUNDING NUMBERS

Job Order No. 573-5094-07
Program Element No. 0603207N
Project No. X0513
Task No.
Accession No. DN259002

6. AUTHOR(S)

E. Joseph Metzger, Robert C. Rhodes, Dong Shan Ko, and Harley E. Hurlburt

7. PERFORMING ORGANIZATION NAME(S) AND ADDRESS(ES)

Naval Research Laboratory
Oceanography Division
Stennis Space Center, MS 39529-5004

8. PERFORMING ORGANIZATION REPORT NUMBER

NRL/FR/7323--97-9673

9. SPONSORING/MONITORING AGENCY NAME(S) AND ADDRESS(ES)

Space and Naval Warfare Systems Command
PMW 185-3B, 24451 Crystal Drive
Arlington, VA 22245-5200

10. SPONSORING/MONITORING AGENCY REPORT NUMBER

11. SUPPLEMENTARY NOTES

12a. DISTRIBUTION/AVAILABILITY STATEMENT

Approved for public release; distribution unlimited.

12b. DISTRIBUTION CODE

13. ABSTRACT *(Maximum 200 words)*

The components of OCEANS 1.0 are described in this report. They consist of the marginally eddy-resolving 1/4° global, reduced gravity NRL (Naval Research Laboratory) Layered Ocean Model (NLOM) and the Pacific West Coast (PWC) model. The reduced gravity version of NLOM is capable of accurately depicting the large-scale oceanic circulation, but there are a few exceptions. The version of NLOM described here is wind-forced only, with no assimilation of altimeter or infrared frontal data. Thus, it cannot be expected to produce accurate hindcasts of sea surface height or upper layer velocities in regions dominated by mesoscale flow instabilities. Maps are provided to show the relative importance of direct wind forcing (deterministic) versus flow instabilities (nondeterministic). NLOM has mixed success in hindcasting sea level variations when compared to observed tide gauges; however, some of its highest correlations are at stations within the PWC domain. A comparison between observed and NLOM simulated drifting buoys has also been made. Ensemble forecasts of four model simulations generally produce an average simulated track that is closer to the observed drifter than any single simulation. However, the model cannot consistently beat a persistence forecast due to the large amount of nondeterminism in the upper layer velocity fields. NLOM will also provide boundary conditions for the PWC model. Two PWC simulations were run, one using climatologically wind-forced NLOM boundary conditions and one using interannually wind-forced NLOM boundary conditions. The latter case showed improved sea level correlation over the former case. Satellite altimetry assimilation and a refinement in the boundary condition implementation should further improve the results. Due to

14. SUBJECT TERMS	15. NUMBER OF PAGES
ocean models, military oceanography, data assimilation	34
	16. PRICE CODE

17. SECURITY CLASSIFICATION OF REPORT	18. SECURITY CLASSIFICATION OF THIS PAGE	19. SECURITY CLASSIFICATION OF ABSTRACT	20. LIMITATION OF ABSTRACT
Unclassified	Unclassified	Unclassified	Same as report

the limitations in physics of the 1/4° reduced gravity NLOM and the lack of satellite data assimilation, it is recommended that OCEANS 1.0 not enter operational check/test mode. A 1/4° thermodynamic finite depth version of NLOM with satellite altimeter assimilation is now available and running in real time at the Fleet Numerical Meteorology and Oceanography Center and it is recommended that this version be implemented. Additionally, further refinement of the boundary condition coupling scheme will improve the transfer of information from the global model to the regional model.

CONTENTS

VALIDATION TEST REPORT FOR OCEANS 1.0: THE 1/4° GLOBAL, REDUCED GRAVITY NRL LAYERED OCEAN MODEL

1.0 INTRODUCTION

The NRL (Naval Research Laboratory) Layered Ocean Model (NLOM) has been under development since 1976 (Hurlburt and Thompson 1980; Wallcraft 1991; Moore and Wallcraft 1996; Wallcraft and Moore 1996). NLOM is the centerpiece of the Ocean Circulation, Evolution, Analysis, and Nowcast System (OCEANS) that is a progression of planned ocean nowcast/forecast systems that will be delivered for naval operations. Increases in computer power over this time frame have led to research versions that are eddy resolving on the global and basin domains. A global model, OCEANS 1.0, has been prepared for transition to the Fleet Numerical Meteorology and Oceanography Center (FNMOC). This is the first planned transition leading to a full eddy-resolving global capability including full data assimilation by the year 2001.

Operational uses for the OCEANS 1.0 system will be to provide improved prediction of surface currents for search and rescue (SAR) and to provide boundary conditions to coastal models planned for operations at FNMOC or the Naval Oceanographic Office. The future versions of OCEANS will include full data assimilation that should also provide useful information for monitoring and prediction of three-dimensional (3-D) temperature and salinity fields that will be used to calculate sound speed. Future systems will be eddy resolving (1/8° or higher), which will allow predictions of major front and eddy systems like the Gulf Stream and Kuroshio Extension.

FNMOC has an immediate requirement for OCEANS 1.0 to provide boundary conditions to a model for the west coast of the United States. This model is a version of the Princeton model, which was set up for the Pacific West Coast (PWC) in a joint project between NRL and FNMOC. A first-generation nesting algorithm has also been developed to use boundary conditions from OCEANS 1.0 as input to PWC. With further refinement, this nesting algorithm could also be used in other areas of the global ocean where the Princeton model is applied to coastal regions. Assimilation of satellite altimeter data should also improve the system for both SAR applications and in providing the boundary conditions for PWC.

This report will discuss the various system components, including PWC, and some of the early validation results for OCEANS 1.0. Comparisons with Pacific Ocean tide gauge sea level data will be shown for NLOM and at west coast stations for PWC. The value added of using OCEANS 1.0 boundary conditions in PWC will be discussed. Also, comparisons with drifting buoys were done to assess the skill of OCEANS 1.0 in nowcasting surface currents. Some additional validations will be shown and recommendations for future systems, including the possibility of using ensemble forecasts, will be made. The results are based on initial validations and much more needs to be done as part of the operational implementation of the system.

2.0 SYSTEM COMPONENTS

2.1 NRL Layered Ocean Model

The NRL Layered Ocean Model is a descendent of the primitive equation model by Hurlburt and Thompson (1980). Since then, the capability of the model has been greatly expanded (Wallcraft 1991; Moore and Wallcraft 1996; Wallcraft and Moore 1996). It is available in both reduced gravity versions, where the lowest layer is infinitely deep and at rest, and in finite depth versions that allow for realistic bottom topography. Results from a 5.5 active layer **reduced gravity** version are discussed here.

The model has a global domain that extends from 72° S to 65° N. The horizontal resolution of each model variable is 1/4° in latitude by 45/128° in longitude. At this resolution, the model is marginally eddy resolving. The model is thermodynamic and horizontal density gradients within an active layer can be modified by advection, diffusion, entrainment, or relaxation to an annual mean density climatology such as Levitus (1982). The model equations and additional details concerning NLOM can be found in Hurlburt et al. (1996b), Metzger and Hurlburt (1996), Moore and Wallcraft (1996), and Shriver and Hurlburt (1997).

The model was originally spun up at 1/2° resolution using the Hellerman and Rosenstein (HR) (1983) monthly wind stress climatology. Initially, the unaltered FNMOC NOGAPS (Navy Operational Global Atmospheric Prediction System) surface wind stresses were used to drive NLOM, but unrealistic current patterns in some regions caused the hybrid approach to be used. This consisted of a combination of the FNMOC NOGAPS and HR surface stresses where the long-term mean (July 1990 to June 1995) was subtracted from the FNMOC stresses and replaced with the HR annual mean. This hybrid approach has been used successfully with the HR and European Centre for Medium-Range Weather Forecasts (ECMWF) 1000 mb winds (Metzger et al. 1992, 1994; Hurlburt et al. 1996b).

After reaching statistical equilibrium at 1/2°, the model was continued at 1/4° resolution using HR stresses until equilibrium was reached. From this point, the 12-hourly FNMOC NOGAPS/HR hybrid winds were used to force the model over the 1990–1996 time frame, which is the period covered in this test report. Four simulations that differ only in the initial state from the climatological spin-up run were integrated during 1990–1996 to differentiate the deterministic and nondeterministic oceanic responses to atmospheric forcing. Additionally, the model was brought up to near real time and transitioned to FNMOC for insertion into their operational run-stream.

2.2 Pacific West Coast Model

The PWC model is a coastal model based on the Princeton Ocean Model (Blumberg and Mellor 1987). It covers a region from the coast seaward to 135° W and from 30° to 49° N. The model has 1/12° (about 10 km) horizontal resolution, which is exactly three times that of the 1/4° global NLOM. There are 30 sigma levels in the vertical. The levels are unevenly spaced with closer spacing near the surface and bottom to resolve the important Ekman flow near shore. The model bottom topography was obtained from the Navy DBDB5 (Digital Bathymetry Data Base at 5′) with mild smoothing and adjustment. The model climatology and the initial temperature and salinity were taken from the Navy's Generalized Digital Environmental Model (GDEM) oceanic climatology (Teague and Hogan 1989; Teague et al. 1990). Since salinity has been shown to be important in the region (Batteen et al. 1995), the coastal model included all seven major rivers that drain into the model's domain. An active river scheme was applied that prescribes, instead of salt flux, the

depth-average velocity according to the monthly fresh water runoff. A data assimilation capability has been added to the later version of model to assimilate multichannel sea surface temperature (MCSST) data.

The PWC model is driven by insertion of information via one-way coupling from the 1/4° global NLOM at the coastal model open boundaries. Two important global model variables, the vertically integrated velocity (transport) and the sea surface elevation, have been used in the coupling. Other global model variables such as density and baroclinic (or 3-D) velocity are not used in the present version of the PWC model. The addition of these variables in the next generation coupling methodology should improve the boundary condition communication between NLOM and PWC. The scheme that utilizes all the global model variables is presented here and the following equations are for a boundary condition with coupling at the southern boundary. With appropriate notation and sign changes they are applied to the western and northern open boundaries.

The boundary condition for the vertically integrated (or external mode) velocity v, normal to the boundary, is prescribed by

$$\frac{dv}{dt} + C\frac{dv}{dy} = \frac{1}{T_s} F\left(\frac{r}{R_s}\right)(v_g^* - v) \tag{1}$$

at the boundary, and from the boundary toward the model interior,

$$\frac{dv}{dt} + \frac{1}{T_s} F\left(\frac{r}{R_s}\right)(v_g^* - v)\,. \tag{2}$$

The left-hand side of Eq. (1) is a radiational boundary condition, where $C = \sqrt{gH}$ is the gravity wave speed, g is the acceleration due to gravity, and H is the water depth. On the right-hand side (RHS) of Eqs. (1) and (2), $1/T_s$ is a nudging parameter, where T_s may be defined as a time scale. The function F defines a "flow relaxation'' parameter, where r is the distance from the open boundary and R_s is a length scale. A Gaussian function was used to define the relaxation parameter

$$F\left(\frac{r}{R_s}\right) = e^{-\left(\frac{r}{R_s}\right)^2}\,. \tag{3}$$

The adjusted global model normal velocity v_g^* is an optimal estimation (Flather 1976) of the vertically integrated velocity estimated from the global model velocity and sea surface elevation

$$v_g^* = v_g + \sqrt{\frac{g}{H}}\,(\eta_g - \eta)\,, \tag{4}$$

where v_g is the vertically integrated velocity computed by integrating global model layer velocity over the layer thickness from the surface to the bottom defined in the coastal model. The term $\eta_g - \eta$ is the difference of the surface elevation between the global model and the coastal model. The global model sea surface elevation η_g was derived from the deviation of global model layer thickness.

For the vertically integrated velocity u, tangential to the boundary, an advectional boundary condition is used

$$\frac{du}{dt} + v\frac{du}{dy} = 0, \tag{5}$$

where the global model value u_g is used when the advection is positive or flow is into the PWC model domain. Otherwise, the internal PWC model value is used.

Similar schemes (Eqs. (1), (2), and (5)), except that $v_g^* = v_g$ and gravity wave speed $C = \sqrt{g'H}$, where g' is the reduced gravitational constant, can be applied to the 3-D internal velocity. At present, however, the radiational boundary condition RHS of Eq. (1) is 0, has been applied to the normal velocity and in the advection scheme, Eq. (5), tangential velocity $u_g = 0$ when the advection is positive.

For the temperature T and salinity S, the advectional boundary conditions were applied,

$$\frac{dT}{dt} + v\frac{dT}{dy} = 0 \tag{6}$$

$$\frac{dS}{dt} + v\frac{dS}{dy} = 0. \tag{7}$$

The temperature T_g and salinity S_g can be evaluated from the global model density and/or the surface elevation via a synthetic technique (Carnes et al. 1996) and used whenever the flow is into the PWC domain. In this version of PWC, the monthly climatological values from GDEM are used instead of T_g and S_g.

The total transport across the coastal model open boundary may not exactly equal the global model transport due to the interpolation/extrapolation from global model grid to PWC model grid, and also due to the presence of the topography in the PWC model. Additional volume from river runoff in the coastal model, which the global model does not have, requires the adjustment of the coastal model area-average surface elevation to that from the global model. This may not be necessary because by applying Eq. (4), the transport from the global model to PWC model will be self-adjusted and gradually push the surface elevation of the PWC model toward that of the global model.

The coupled PWC model was spun-up with the climatological HR monthly wind stress. The synoptic FNMOC NOGAPS/HR hybrid wind stresses are then used for the surface forcing. Monthly temperature and salinity from GDEM are applied with a relaxation scheme instead of heat and salt fluxes at the surface. MCSST was also tried for the surface heat forcing. The fields predicted by the coastal model are reasonable and reflect the presence of a vigorously meandering California Current System with its associated eddies. The model exhibits many of the known characteristics of oceanographic variability off the U.S. west coast. This includes the annual migration of the California Current, the formation of the Davidson Current and the Southern California Countercurrent, the reversal of coastal current at the Washington-Oregon shelf, the annual cycle of coastal upwelling, and the presence of jets, cold filaments, and eddies near the coast. The active river

scheme also works well. The model vividly presents the seasonal extension and retreat of the river plumes, especially around the Columbia River, which has the largest runoff.

3.0 TESTING RESULTS

3.1 Simulation of the Large-Scale Oceanic Circulation

3.1.1 Position of Currents

Figure 1 shows the 1990–1996 mean sea surface height (SSH) from the combined mean of the four global simulations, while Fig. 2 is the annual mean GDEM dynamic heights relative to 1000 dbar. In the Pacific Ocean (Fig. 1a), the model is able to simulate most of the basic upper-ocean circulation

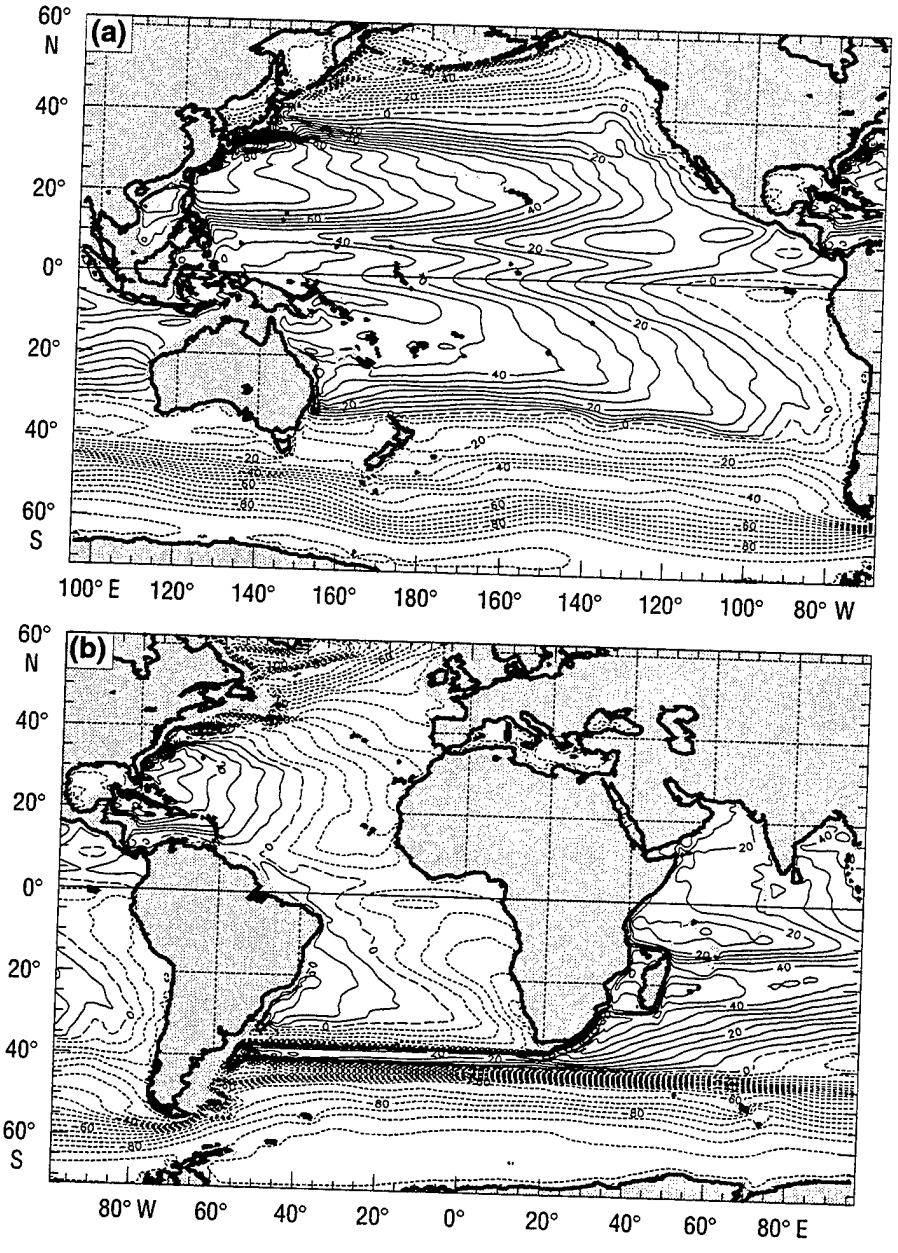

Fig. 1 — The 1990–1996 mean SSH from the NLOM for (a) the Pacific and (b) the Atlantic/Indian hemispheres. Mean is an average of the four NLOM simulations. The contour interval is 5 cm.

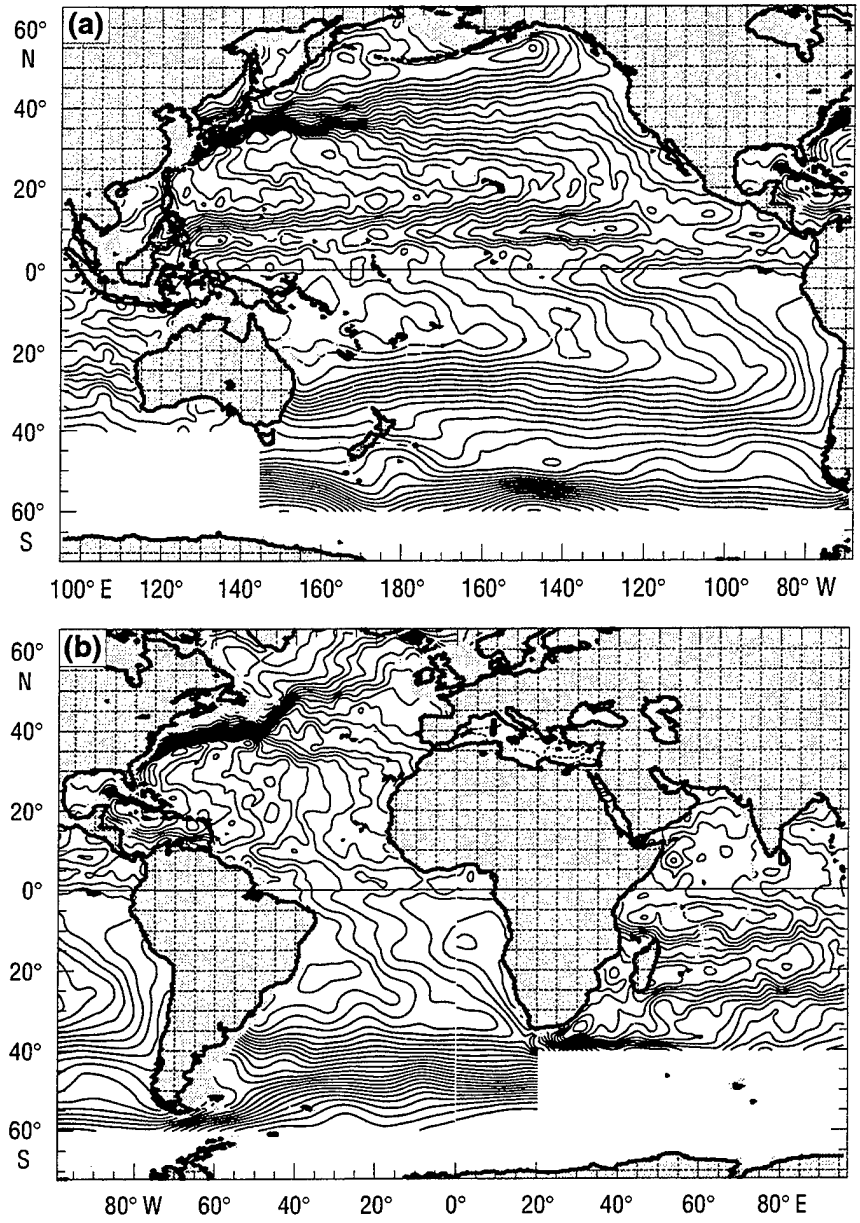

Fig. 2 — Annual mean dynamic height relative to 1000 dbar from the GDEM oceanic climatology (Teague et al. 1990) for (a) the Pacific and (b) the Atlantic/Indian hemispheres. The contour interval is 5 cm. The data have a 9-point spatial smoother applied five times.

patterns. Starting in the Northern Hemisphere (NH), the cyclonic subpolar gyre and anticyclonic subtropical gyre dominate the large scale. The subpolar gyre is bounded by the Alaska Stream on the north, the East Kamchatka Current on the west and the Oyashio Current on the west and southwest. The model's representation of the Oyashio is too diffuse, as it is in the GDEM climatology, due to temporal and spatial sampling. A weak subarctic front/North Pacific Current separates these two gyres along 41°–45° N. The subtropical gyre is bounded by the Kuroshio on the west, the subarctic front on the north, and the North Equatorial Current (NEC) along 10°–18° N on the

south. The model-simulated Kuroshio separates from the Japan coast slightly too far south compared to GDEM, and it is missing the characteristic meanders in the Kuroshio Extension. This is due to the lack of upper ocean – topographic coupling as explained by Hurlburt et al. (1996b). The interior of the model subtropical gyre agrees well with GDEM.

At 14° N, the NEC splits at the Philippines coast into the northward Kuroshio and the southward Mindanao Current (MC). This bifurcation latitude is in close agreement with the GDEM climatology. The MC is the western boundary current of the zonally elongated northern tropical gyre with the NEC on the north and the North Equatorial Countercurrent (NECC) on the south along 5°–10° N. The model SSH gradient across the equatorial Pacific gives about a 50 cm rise from east to west and this agrees with the observed 50 cm rise noted by Philander (1990); GDEM has an approximate 60 cm east-west tilt across the equator.

In the Southern Hemisphere (SH), the South Equatorial Countercurrent is centered at 7°–10° S and is much weaker than the NECC as is observed. The core of this current is confined mostly to the west of the dateline. The Antarctic Circumpolar Current (ACC) is weak in the model and very zonal in part because the reduced gravity formulation does not allow for bottom topography interactions.

In the NH Atlantic Ocean (Fig. 1b), the simulated subtropical gyre only has the C-shape in the extreme western part of the basin, whereas this C-shape signature extends well into the interior in GDEM (Fig. 2b). The model also produces two Gulf Streams, one that separates from the U.S. coast near Cape Hatteras and another that continues along the continental boundary. This unrealistic, two-Gulf-Stream pattern is consistent with linear models that have a Sverdrup (1947) interior closed by viscously dominated western boundary currents as in Munk (1950). This is mostly due to the relatively coarse horizontal resolution and the lack of a deep western boundary current, which is part of the thermohaline circulation. (Finite depth versions of NLOM include this abyssal flow.) Recent work suggests that strong, nonlinear dynamics and a horizontal grid resolution of 1/32° will probably be required for robust Gulf Stream separation at Cape Hatteras (Hurlburt and Hogan 1997).

In the Gulf of Mexico, the model simulates the Loop Current and actively sheds eddies. The North Brazil retroflection is seen near 7° N, 48° W as observed. The model realistically simulates the ring generation characteristic of this region (Fratantoni et al. 1995). Finally, the model does not simulate the Agulhas Retroflection at the southern tip of Africa as seen in GDEM and in a version of the 1/4° global NLOM with realistic bottom topography. In the latter model, the retroflection is produced by a mixed barotropic-baroclinic flow instability and is facilitated by the bottom topography, both of which are missing in the reduced gravity model.

3.1.2 Transport Comparison with Observations

Some selected examples of observational transport estimates are compared against NLOM. The scatter of the data is somewhat high and differences may arise from temporal variability, the varying measurement techniques, the reference levels chosen, and the location of the cross-sections. Nonetheless, they provide a qualitative measure of the accuracy of the ocean model. Table 1 lists model versus observational transport estimates. In most cases, the model was sampled near the observational data location. For the most part, the model transport estimates are within the range of the observed data. The NLOM Atlantic Equatorial Undercurrent values are low because the layer structure is not optimal for this basin.

Table 1 — NLOM Versus Observational Transport Estimates for Selected Sections of the Atlantic and Pacific Ocean. Values are in Sverdrups (1 $Sv = 10^6$ m^3/s). The Model Values are an Average from the Four Simulations.

CURRENT	NLOM	OBSERVED	SOURCE
Pacific			
Kuroshio (east of Luzon)	18	12–31	Toole et al. (1990)
North Equatorial (153° W)	22	23	Wyrtki and Kilonsky (1984)
North Equatorial (130° E)	45	32–61	Toole et al. (1990)
Mindanao (near 8° N)	24	16–26	Lukas et al. (1991)
PACIO throughflow	11	10–20	Lukas et al. (1996)
Equatorial Under (153° W)	38	30	Wyrtki and Kilonsky (1984)
		32	Lukas and Firing (1984)
Atlantic			
Florida (27° N)	34	32	Larson (1992)
Yucatan	27	30	Nowlin (1972)
Equatorial Under (35° W)	10	18	Gouriou and Reverdin (1992)
Equatorial Under (23° W)	6	16	Gouriou and Reverdin (1992)

3.2 Determinism vs. Nondeterminism

Figure 3 a,b shows root-mean-square (RMS) SSH, Fig. 3 c,d shows RMS for the upper layer u-velocity component (U1), and Fig. 3 e,f shows RMS for the upper layer v-velocity component (V1). These fields are computed over the 1990–1996 time frame and are the combined variability from all four experiments. In the Pacific Ocean, the meandering associated with the Kuroshio is clearly evident in the SSH field to the south and east of Japan. Relative SSH maxima are also seen along the latitudes of the NEC, the tropical gyre, and the NECC. Interannual variations in both the strength and position of these features contribute to the SSH variability in addition to meanders and eddies. The high RMS SSH east of the Philippines near 15° N is associated with changes in the NEC bifurcation latitude. A corridor of high RMS SSH also extends westward off the coast of Mexico. These Tehuantepec eddies are generated by an orographically produced, complex wind stress curl pattern along the coast of Mexico.

The highest variability in the upper layer velocity components is in the tropical latitudes, with U1 being dominant over V1. Again, relative maxima in U1 are seen along the NECC and the South Equatorial Current (SEC) at the equator. High V1 variability is mostly along the western boundary of the basin. The Atlantic Ocean SSH variability is much weaker than the Pacific. Relative maxima are seen in the Gulf Stream, Loop Current, and Brazil-Malvinas regions. High U1 and V1 variability is clearly evident at the Brazil retroflection (and along the equatorial latitudes for U1). Variability associated with monsoonal wind forcing is evident in the Arabian Sea and Bay of Bengal in the Indian Ocean for all three model variables.

Because the four 1/4° model simulations are identical except for the initial state, the differences between them should be due to mesoscale flow instabilities. Metzger et al. (1994) developed a technique to separate the total SSH variability field into two components, one caused by direct

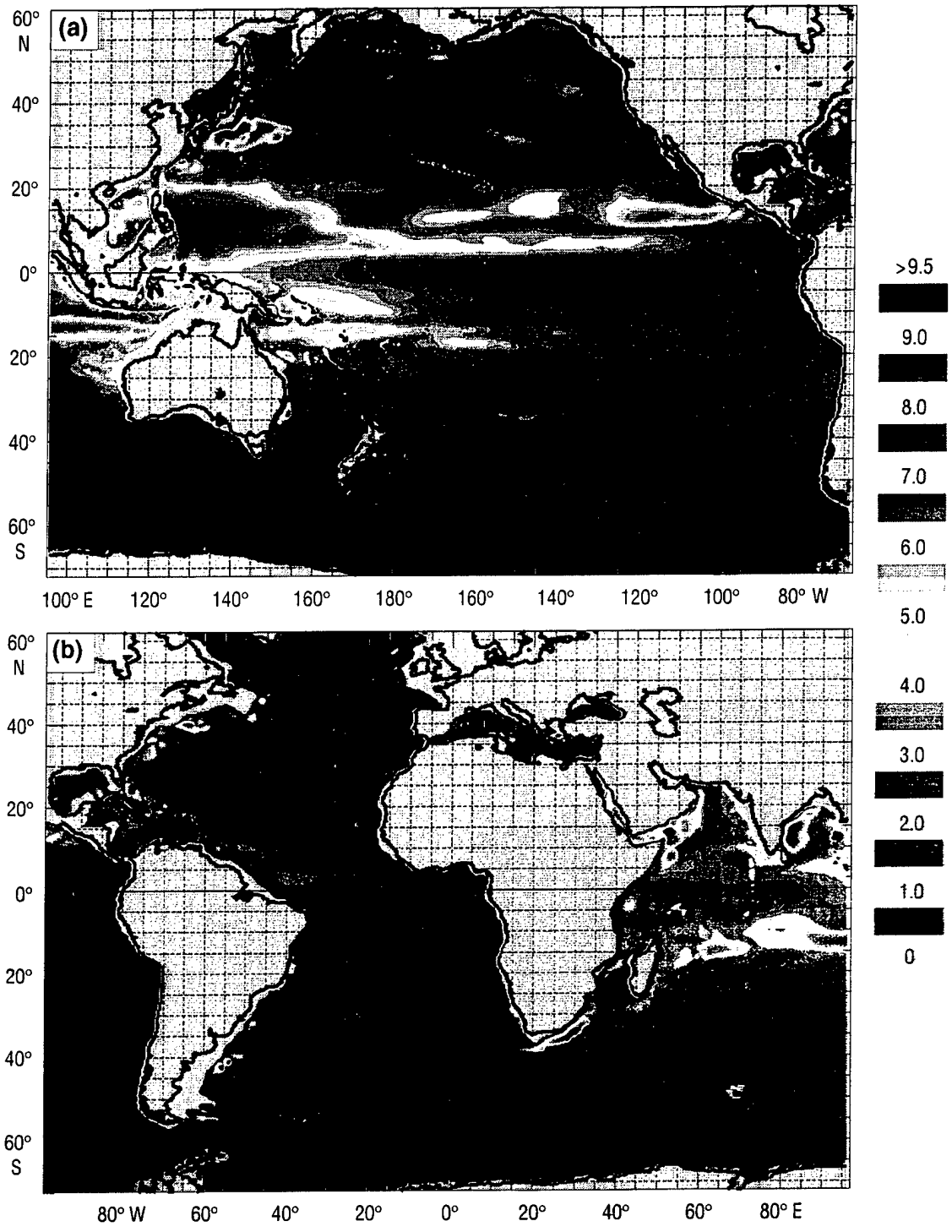

Fig. 3 — The 1990–1996 RMS SSH, U1 and V1, from NLOM for the Pacific hemisphere (a, c, e, respectively) and for the Atlantic/Indian hemisphere (b, d, f, respectively). The contour interval is 0.5 cm for SSH and 0.01 m/s for U1 and V1.

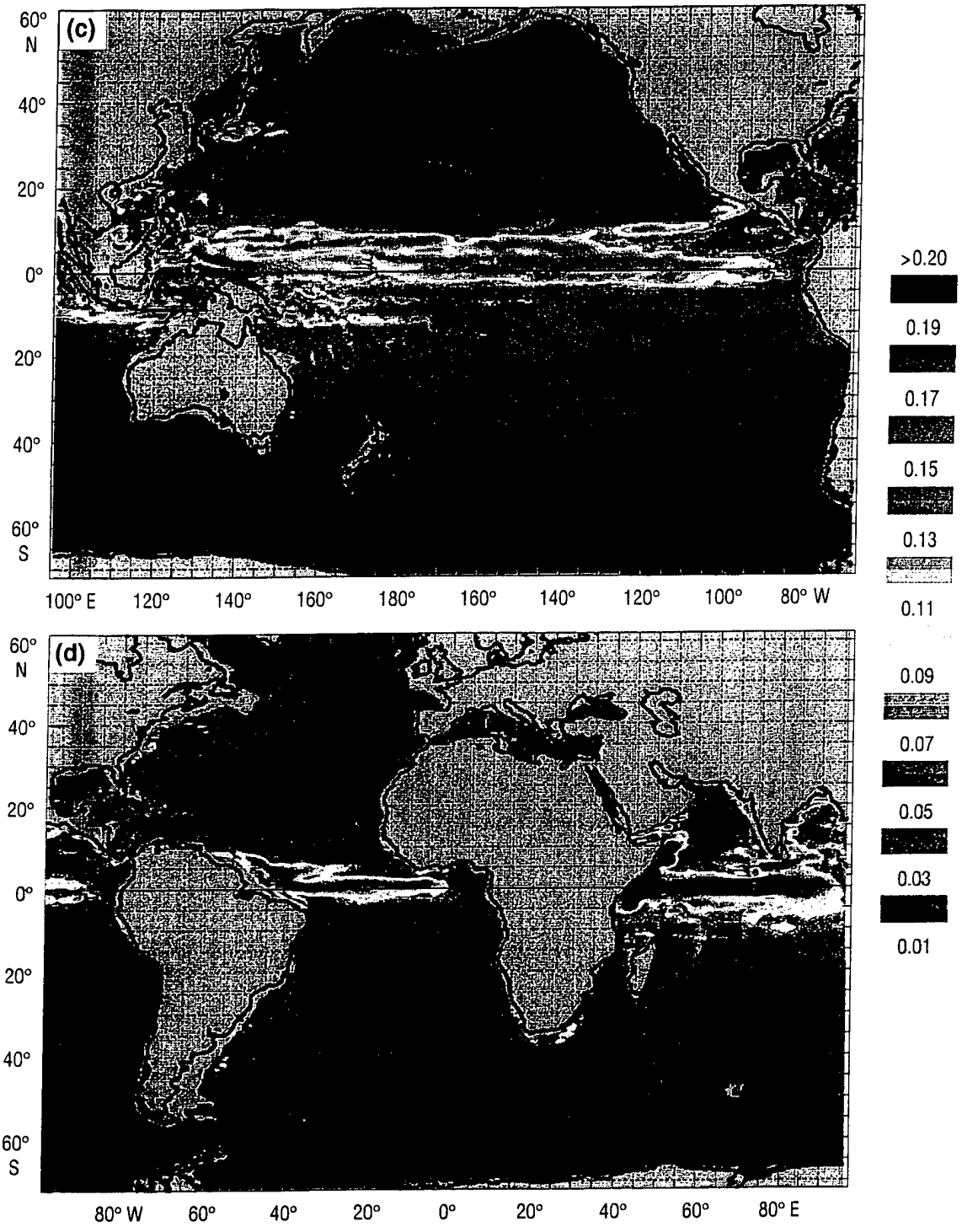

Fig. 3 — Continued

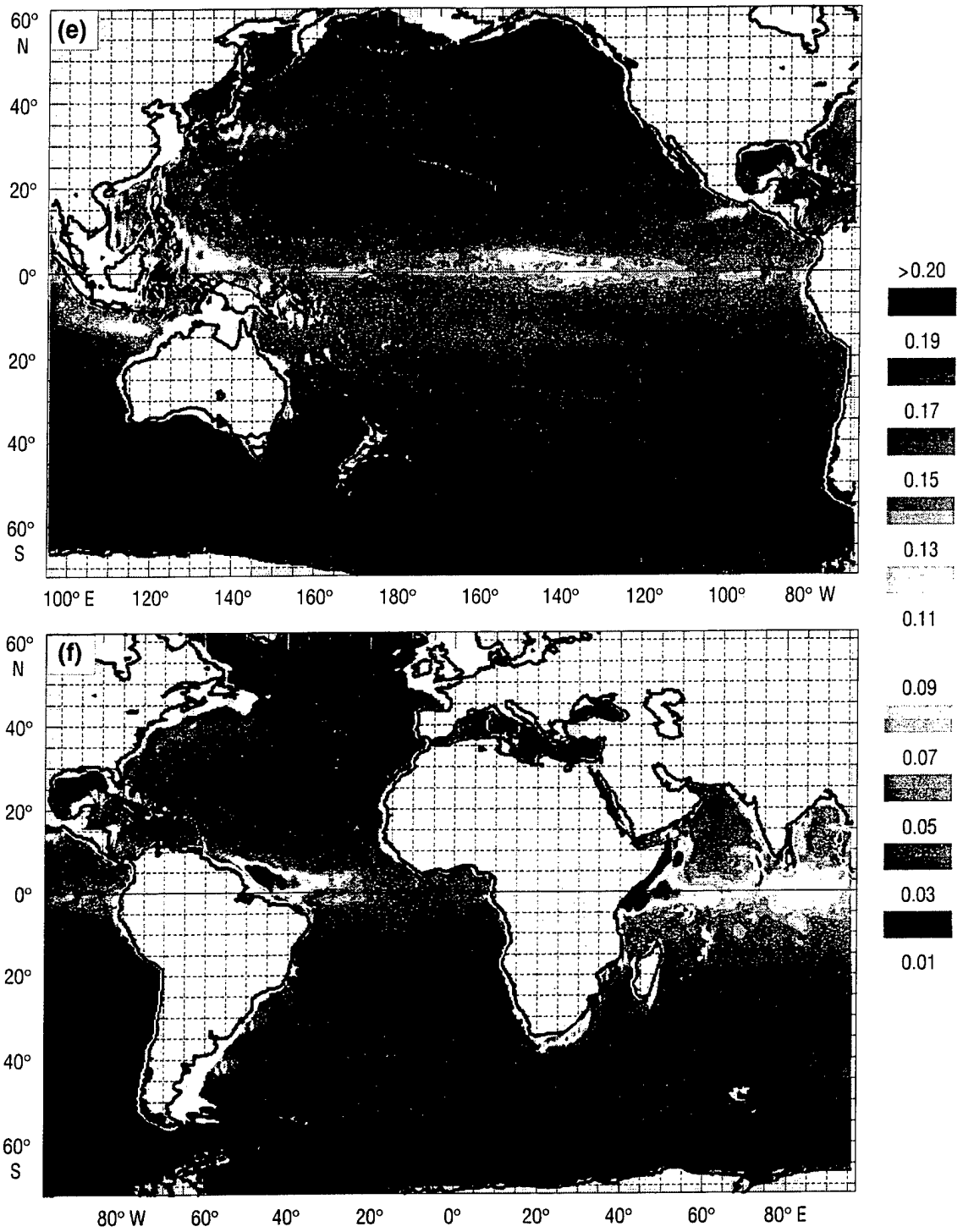

Fig. 3 — Continued

atmospheric forcing (deterministic) and the other due to mesoscale flow instabilities (nondeterministic). However, because of a limited number of realizations, the separation of these two contributions to the temporal SSH variability is not totally complete. The flow instabilities component is *under*-estimated and the wind-forced component is *over*estimated. Analysis from a 1/16° Pacific model (not shown) indicate that upward of five simulations would be required to more accurately depict the nondeterministic contribution. Obviously, the 1/4° global model has fewer flow instabilities, but the 1/16° results highlight the need for numerous simulations. Additional experiments would be needed to test the convergence of this analysis at this model resolution. (To compare the fractional SSH variability using four and two realizations, see Fig. 4 a and g, respectively.) These fields, nonetheless, at least indicate regions where instability mechanisms are important and must be considered when analyzing the wind-forced 1/4° global model.

The relative importance of the two anomaly generation mechanisms is shown in Fig. 4 a,b for SSH, Fig. 4 c,d for U1, and Fig. 4 e,f for V1. Blue areas are regions where variations are controlled largely by the wind forcing, whereas mesoscale flow instabilities are more important in the orange and red areas. In the Pacific Ocean, direct wind forcing is the main SSH anomaly generation mechanism in the tropical latitudes, but flow instabilities dominate the upper layer meridional component, V1. The U1 component is relatively deterministic along a band from the equator to 10° N, even though its RMS is approximately twice as high as V1. This is probably because the zonal component is more geostrophically constrained than the meridional flow. Given the large fraction of nondeterminism in the meridional flow, predicting the upper layer flow across the majority of the tropics and subtropics will be a severe test for the model, even when assimilating altimetry.

The SSH variability is relatively deterministic along the eastern boundaries of the Pacific, and as will be shown, NLOM shows relatively good skill in hindcasting sea level in these regions. Here the Tehauntepec eddies that are generated off the west coast of Mexico (high band of RMS SSH, U1 along 13° N) are a very deterministic feature in the model. Ekman flow is also a deterministic response to wind forcing and this can be seen in the model where the upper layer is thin, namely the subpolar gyre in the Pacific and ACC regions.

In the Atlantic Ocean, the Gulf Stream region is nondeterministic in the SSH and velocity variability as would be expected. The Gulf of Mexico velocity variability is also very nondeterministic and it does not appear to be linked to any nondeterminism in the Caribbean Sea. North of approximately 20° N, the Atlantic SSH variability appears to be relatively nondeterministic, yet relatively deterministic away from the Gulf Stream in the velocity components. This phenomenon is not yet fully understood.

3.3 Island Sea Level Comparison

The Integrated Global Ocean Services System (IGOSS) Sea Level Program makes island and coastal data available in the form of monthly means. The time series represents deviations from the 1975–1986 mean sea level computed for each station; all data have been quality controlled and any large linear trends have been removed. Sea level time series from the model have been extracted at the gridpoints closest to the island/coastal station. Since the model land/sea boundary is the 200 m isobath, the sampling points may differ by up to a few degrees, a point to consider in comparing the results. The long-term mean has also been subtracted from the model sea level time series.

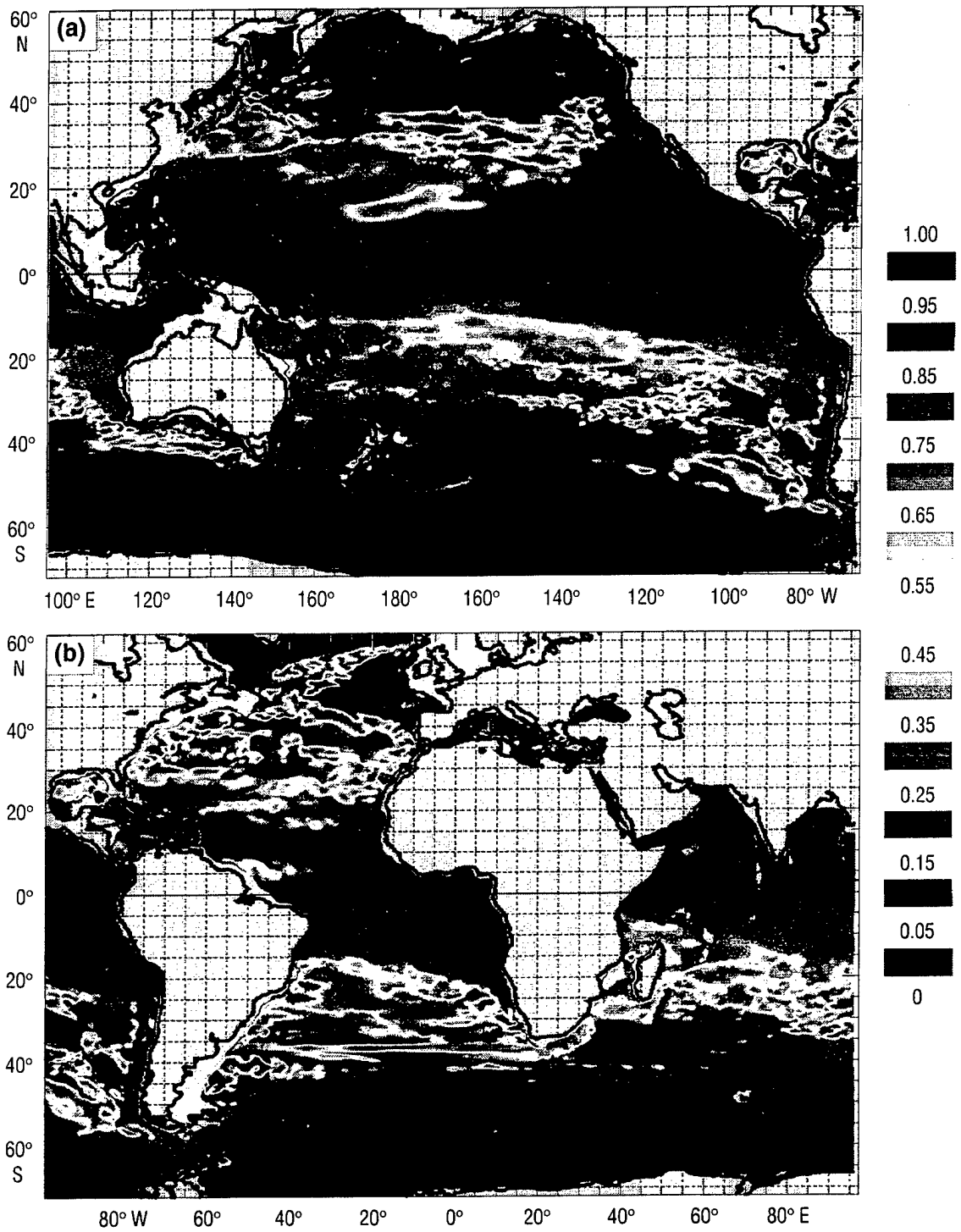

Fig. 4 — Fraction of the simulated variability in the 1/4° global NLOM caused by direct wind forcing (deterministic–blue areas) and by flow instabilities (nondeterministic–red areas) for SSH, U1, and V1 in the Pacific hemisphere (a, c, e, respectively) and the Atlantic/Indian hemisphere (b, d, f, respectively). Panels a–f are calculated using four model realizations. Panel g is the fraction of simulated SSH variability for the Pacific hemisphere using two model realizations.

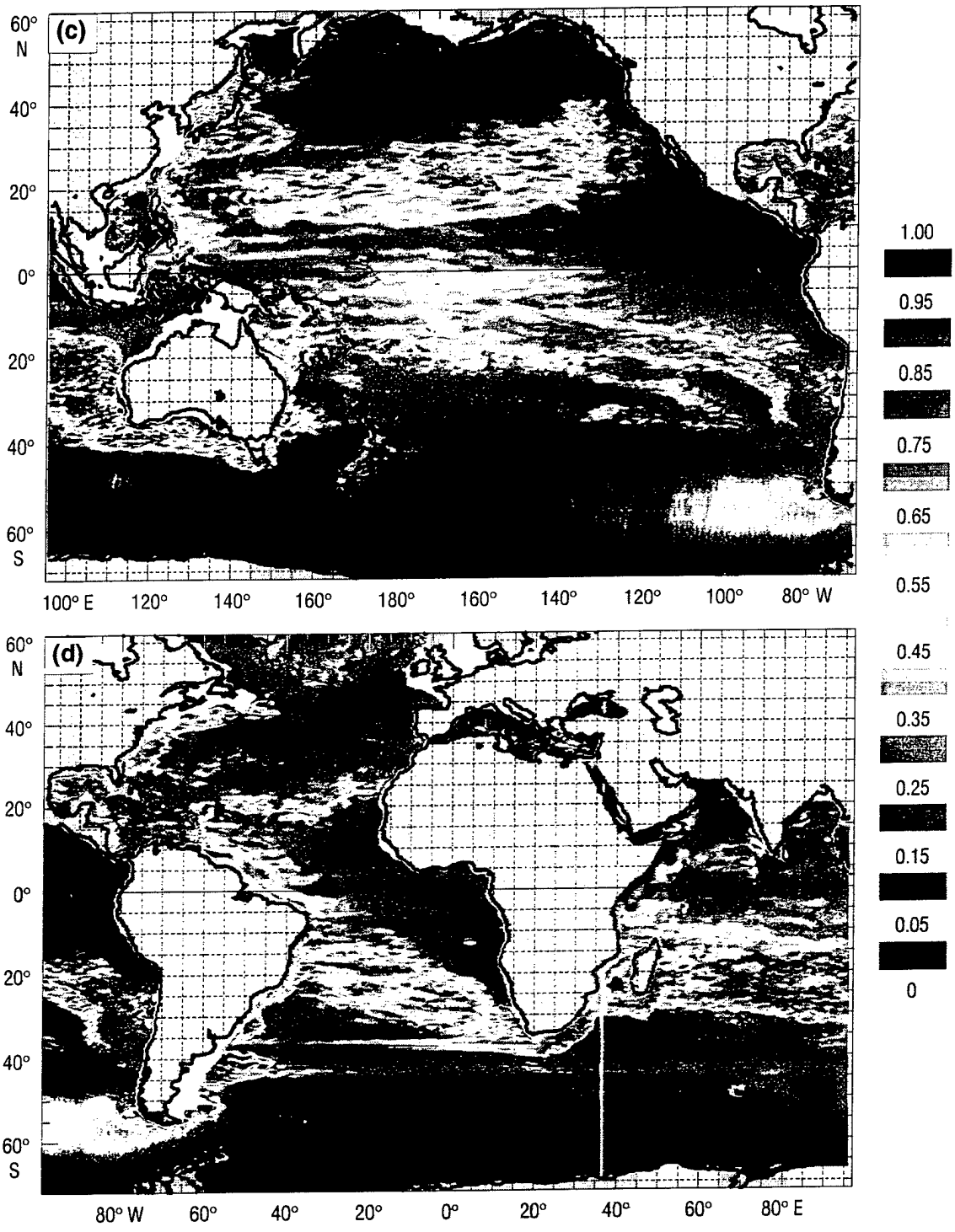

Fig. 4 — Continued

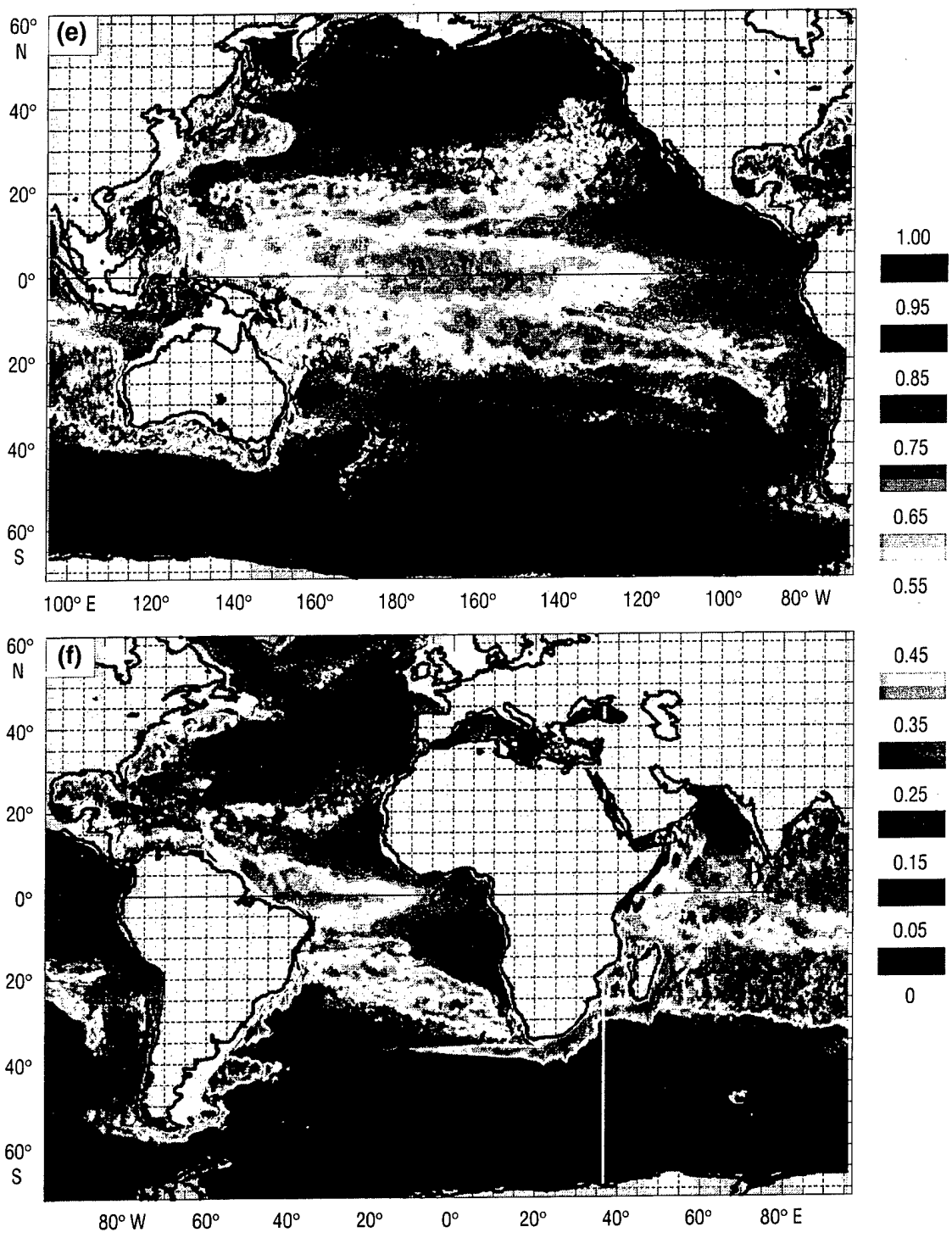

Fig. 4 — Continued

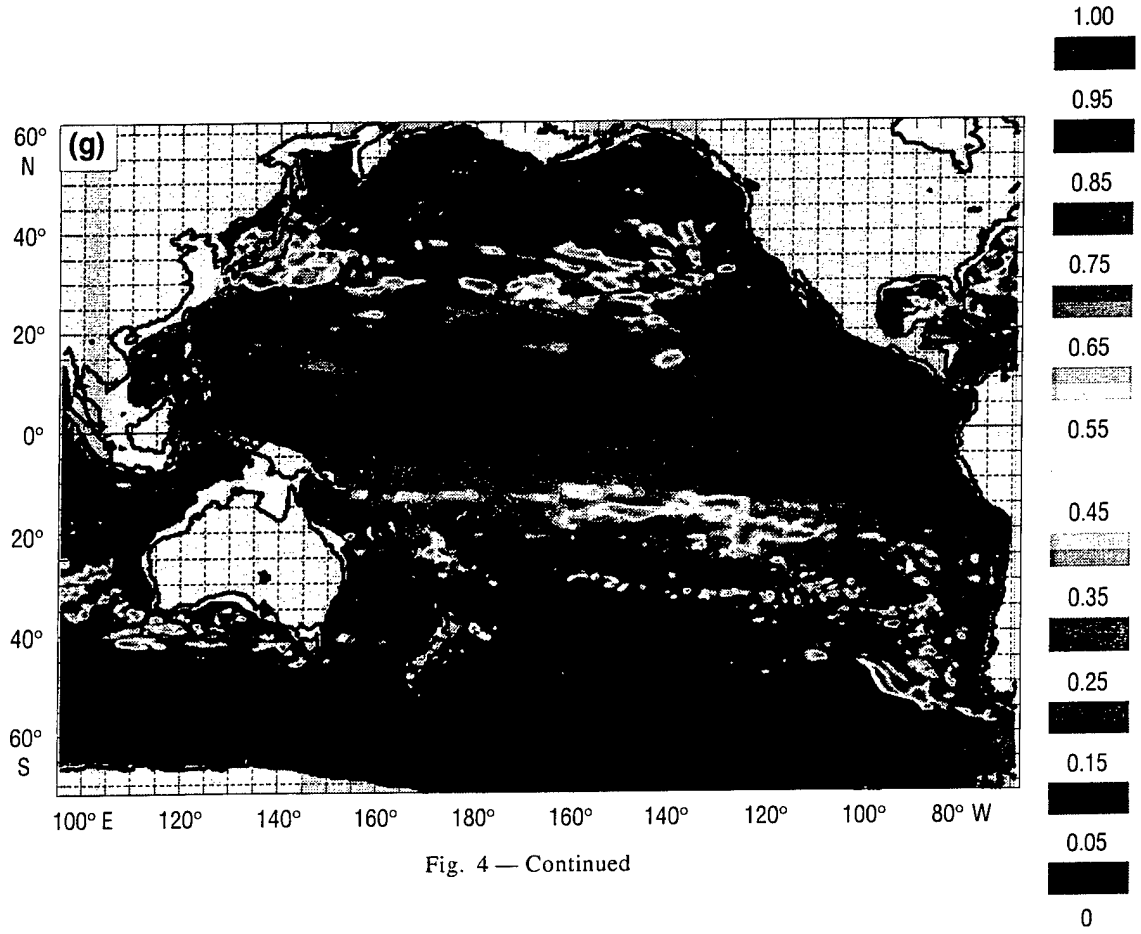

Fig. 4 — Continued

Comparisons between the four global simulations and the observed IGOSS monthly sea level data were conducted at 69 island and coastal stations in the Pacific. The majority of stations are within the tropical latitudes, but a number exist in mid-latitude and subpolar regions. Correlations between an average of the four model simulations and the observed sea level were computed over 1991–1996 (Tables 2 and 3). The 1990 data were excluded from the analysis because of potential numerical noise that may have been generated in the switch between climatological monthly and 12-hourly hindcast winds. An average of the four simulations should also reduce the flow instability effects somewhat. The last column in these tables is for a similar version of NLOM, but the correlations are for an average of two simulations forced with ECMWF/HR hybrid winds. They are included for comparison with the FNMOC/HR experiments.

In the northwest Pacific, most correlations for the Japanese stations are negative. Here, the model SSH variability is much less than observed as it lacks a strong seasonal signal, in part due to the lack of a steric signal due to heating and cooling. (This version of NLOM can use time dependent thermal forcing and produce the associated steric anomalies, but it was not included in these experiments.) However, without a full data assimilative system, which included both altimetry assimilation and rubber sheeting of frontal infrared (IR) data, a solely wind-forced model would not be expected to predict SSH variability with much skill in this region due to mesoscale flow instabilities (Fig. 4 a,c,e).

The model produces some of its highest correlations along the U.S./Canadian west coast, which is within the domain of the PWC model. Figure 4a also indicates this as a region of relatively

Table 2 — The 1991–96 Correlation Coefficients Between Observed IGOSS Sea Level Data and an Average of the Four 1/4° Global NLOM Simulations Forced with FNMOC/HR Hybrid Winds (column three) and an Average of Two 1/4° Global NLOM Simulations Forced with ECMWF/HR Hybrid Winds (column four). The IGOSS Data are Monthly Averages and a 30-d Running Mean has been Applied to the Model Results.

IGOSS STATION	LOCATION (Lat., Long.)	1/4° NLOM FNMOC/HR	1/4° NLOM ECMWF/HR
Northwest Pacific			
Naha, Japan	26°13′ N, 127°40′ E	0.67	0.15
Chichijima, Japan	27°05′ N, 142°11′ E	0.03	0.02
Aburatsu, Japan	31°34′ N, 131°25′ E	–0.06	–0.06
Kushimoto, Japan	33°28′ N, 135°47′ E	–0.18	–0.11
Mera, Japan	34°55′ N, 139°50′ E	–0.26	–0.03
Fukaura, Japan	40°39′ N, 139°56′ E	–0.32	–0.06
Kushiro, Japan	42°58′ N, 144°23′ E	–0.19	–0.27
Wakkanai, Japan	45°25′ N, 141°41′ E	–0.49	–0.37
Petropavlovsk, Russia	53°01′ N, 158°38′ E	0.46	0.28
Northeast Pacific			
Adak, Alaska	51°51′ N, 176°39′ W	–0.02	–0.19
Unalaska, Alaska	53°53′ N, 166°00′ W	0.19	0.08
Seldovia, Alaska	59°26′ N, 151°43′ W	0.23	0.27
Seward, Alaska	60°05′ N, 149°27′ W	0.13	0.18
Yakutat, Alaska	59°33′ N, 139°44′ W	0.29	0.39
Sitka, Alaska	57°03′ N, 135°20′ W	0.51	0.62
Prince Ruppert, Canada	54°19′ N, 130°20′ W	0.58	0.68
Tofino, Canada	49°09′ N, 125°55′ W	0.78	0.87
Bamfield, Canada	48°50′ N, 125°08′ W	0.80	0.88
Neah Bay, Washington	48°22′ N, 124°37′ W	0.82	0.88
Crescent City, California	41°45′ N, 124°12′ W	0.82	0.82
San Francisco, California	37°48′ N, 122°28′ W	0.66	0.76
San Diego, California	32°42′ N, 117°10′ W	0.49	0.52
West Equatorial Pacific			
Wake, USA Trust	19°17′ N, 166°37′ E	0.30	0.14
Saipan, North Mariana	15°14′ N, 145°45′ E	0.34	0.27
Guam, Marianas	13°26′ N, 144°39′ E	0.67	0.37
Legaspi, Philippines	13°09′ N, 123°45′ E	0.30	0.43
Davao, Philippines	7°05′ N, 125°38′ E	0.58	0.38
Kwajalein, Marshall	8°44′ N, 167°44′ E	0.76	0.46
Yap, F. S. M.	9°31′ N, 138°08′ E	0.65	0.57
Pohnpei, F. S. M.	6°59′ N, 158°14′ E	0.72	0.75
Kapingamarangi, F. S. M.	1°06′ N, 154°47′ E	0.76	0.81
Malakal, Belau	7°20′ N, 134°28′ E	0.46	0.50
Nauru, Nauru	0°32′ S, 166°54′ E	0.58	0.76
Rabaul, P. N. G.	4°12′ S, 152°11′ E	0.94	0.88
Honiara, Solomons	9°26′ S, 159°57′ E	0.85	0.84

Table 3 — The 1991–1996 Correlation Coefficients Between Observed IGOSS Sea Level Data and an Average of the Four 1/4° Global NLOM Simulations Forced with FNMOC/HR Hybrid Winds (column three) and an Average of Two 1/4° Global NLOM Simulations Forced with ECMWF/HR Hybrid Winds (column four). The IGOSS Data are Monthly Averages and a 30-d Running Mean has been Applied to the Model Results.

IGOSS STATION	LOCATION (Lat., Long.)	1/4° NLOM FNMOC/HR	1/4° NLOM ECMWF/HR
Central Equatorial Pacific			
Midway, USA Trust	28°13′ N, 177°22′ W	0.13	–0.01
French Frigate Shoal, Hawaii	23°52′ N, 166°17′ W	–0.02	–0.39
Honolulu, Hawaii	21°18′ N, 157°52′ W	0.39	0.13
Hilo, Hawaii	19°44′ N, 155°04′ W	–0.03	–0.07
Johnston, USA Trust	16°45′ N, 169°31′ W	0.23	0.11
Majuro, Marshall	7°06′ N, 171°22′ E	0.62	0.60
Christmas, Kiribati	1°59′ N, 157°29′ W	0.70	0.86
Tarawa, Kiribati	1°22′ N, 172°56′ E	0.53	0.83
Kanton, Kiribati	2°49′ S, 171°43′ W	0.49	0.72
Funafuti, Tuvalu	8°31′ S, 179°12′ E	0.63	0.77
Nuku Hiva, French Polynesia	8°56′ S, 140°05′ W	0.20	0.19
Penrhyn, Cook Island	9°01′ S, 158°04′ W	0.61	0.45
Pago Pago, Samoa	14°17′ S, 170°41′ W	0.15	0.47
Papeete, French Polynesia	17°32′ S, 149°34′ W	0.04	–0.14
Suva, Fiji	18°08′ S, 178°26′ E	0.05	0.27
Rarotonga, Cook Island	21°12′ S, 159°46′ W	–0.11	–0.09
Rikitea, French Polynesia	23°08′ S, 134°57′ W	0.15	0.33
East Equatorial Pacific			
Cabo San Lucas, Mexico	22°53′ N, 109°54′ W	0.32	0.36
Quepos, Costa Rica	9°24′ N, 84°10′ W	0.39	0.74
Buenaventura, Colombia	3°54′ N, 77°06′ W	0.58	0.80
Baltra, Ecuador	0°26′ S, 90°17′ W	0.72	0.76
Santa Cruz, Ecuador	0°45′ S, 90°19′ W	0.72	0.77
Callao, Peru	12°03′ S, 77°09′ W	0.73	0.64
Southwest Pacific			
Townsville, Australia	19°16′ S, 146°50′ E	0.22	–0.09
Noumea, New Caledonia	22°18′ S, 166°26′ E	0.33	0.08
Bundaberg, Australia	24°50′ S, 152°30′ E	0.10	–0.11
Sydney, Australia	33°51′ S, 151°14′ E	0.50	0.31
Auckland, New Zealand	36°00′ S, 174°50′ E	0.31	0.40
Wellington, New Zealand	41°17′ S, 174°47′ E	0.47	0.50
Southeast Pacific			
Easter, Chile	27°09′ S, 109°27′ W	0.16	–0.14
Antofagasta-BM45, Chile	23°39′ S, 70°24′ W	0.44	0.31
Caldera, Chile	27°04′ S, 70°50′ W	0.24	0.53
Valparaiso, Chile	33°02′ S, 71°38′ W	0.25	0.54
Talcahuano, Chile	36°42′ S, 73°06′ W	0.58	0.58

deterministic SSH variability. Figure 5 shows the model versus observed SSH for four stations within this region. For these monthly data, the seasonal cycle is clearly the dominant signal. The phase agrees well between NLOM and the observed data, but the variability of the model is slightly weaker than the IGOSS data. The Gulf of Alaska correlations are low, due mostly to phase errors, although they are high in other NLOM simulations using ECMWF/HR hybrid wind forcing, such as the 1/8° Pacific NLOM with realistic bottom topography (Hurlburt et al. 1996a; Smedstad et al. 1997).

At the equatorial stations, the model has mixed success. Those stations within approximately 3° of the equator generally have correlations greater than 0.5. An examination of Fig. 4a reveals that if even a small portion of the SSH variability is the result of flow instabilities (nondeterministic), the correlation between the model and observed data can be low. Most of the near equatorial stations do not have a strong observed seasonal signal, but the model SSH variability is comparable in magnitude. Other sources of errors may be related to the wind forcing, e.g., the latitudinal migration of the tropical gyre systems is very wind dependent. Spatial or temporal wind errors could displace the equatorial current systems enough to produce large differences between observed and simulated sea level.

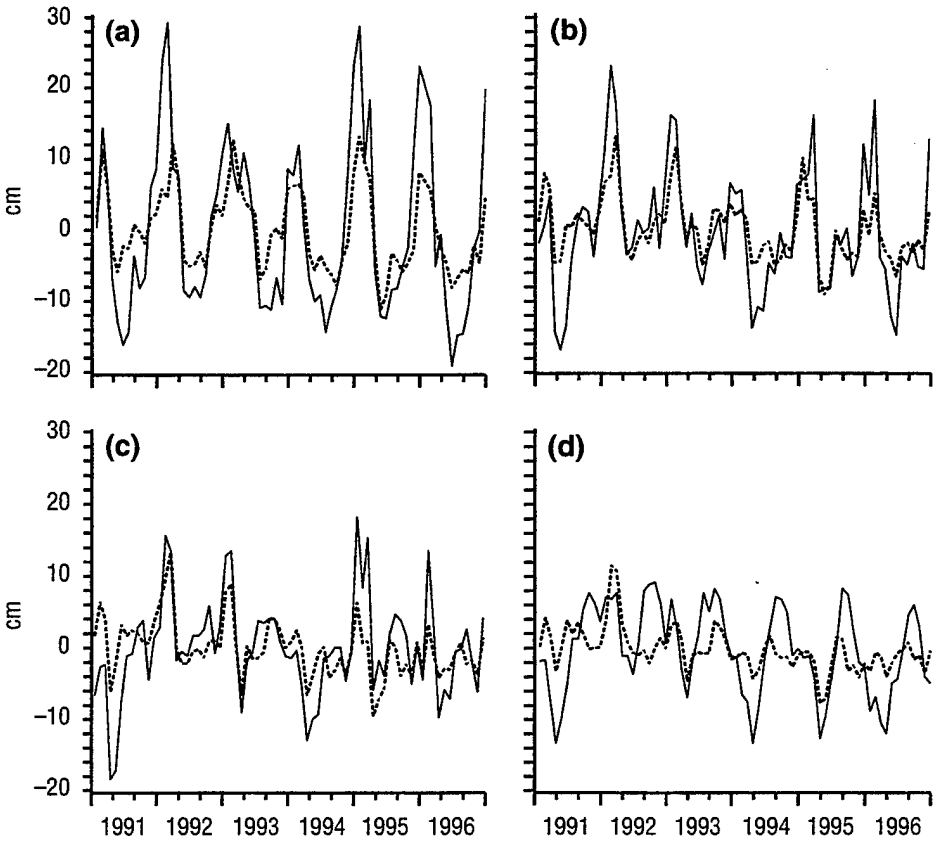

Fig. 5 — Observed monthly IGOSS versus NLOM simulated sea level for four stations within the PWC domain: (a) Neah Bay, WA, (b) Crescent City, CA, (c) San Francisco, CA, and (d) San Diego, CA. The correlation coefficients are 0.82, 0.82, 0.66, and 0.49, respectively. IGOSS data are the solid curves and the model results are dashed. A 30-d running mean has been applied to the model output.

The correlations in the southwest and southeast Pacific are also low. In the southwest Pacific, the model produces a weak seasonal signal (as in the northwest), but in the southeast Pacific, the seasonal signal is weak in both the observations and the model. The strong upwelling associated with coastally trapped Kelvin waves is not as evident at these SH stations.

Hurlburt et al. (1996a) and Smedstad et al. (1997) discuss the impact of assimilating altimeter data into a 1/8° Pacific NLOM in relation to correlation improvements between the IGOSS and model-simulated sea level. The impact of the altimetric data assimilation is the most substantial, where the skill of the wind-driven model is relatively low and the space-time scales of the variations are sufficiently resolved by the altimeter data. The subtropical gyre region, and in the tropics a few degrees away from the equator, exhibit the greatest improvement. Altimetric data assimilation did not greatly improve sea level correlations near Japan because of the relatively small time and space scales, but it did improve the ability of the model to represent observed meanders in the Kuroshio pathway as verified by comparison to satellite IR images. While altimetric data assimilation was not performed in the 1/4° global **reduced gravity** model detailed here, it is currently in the 1/4° global **finite depth** model now running in real time at FNMOC.

3.4 Drifting Buoy Comparison

A set of World Ocean Circulation Experiment (WOCE) and Tropical Ocean and Global Atmosphere (TOGA) drifting buoys has been obtained from Peter Niiler (University of California-San Diego) that provides mixed layer velocity observations on a basin-wide scale. The buoys have a drogue centered at 15 m, have been quality controlled, and are temporally interpolated to the 6-hourly synoptic times. Buoys that lost their drogues were excluded as part of the quality control checks. The vast majority of the WOCE/TOGA drifting buoys are located in the Pacific Ocean. A very small subset of these has been chosen for comparison with NLOM. Most buoys had lifespans of at least 6 mo.

NLOM is capable of simulating drifting buoys during runtime or from model history files. A subset of 19 randomly chosen WOCE/TOGA buoys, distributed across the Pacific Ocean, were seeded in the upper layer (rest thickness = 80 m) of the model during runtime. After 30 d, the simulated buoys were redeployed coincident with the WOCE/TOGA drifter locations. Separation distance between the observed and model-simulated drifters was calculated and compared against a forecast of persistence (no movement).

Comparison of observed and model-simulated drifting buoys is a severe test for NLOM, even against a persistence forecast. A number of factors can cause large discrepancies between the two tracks. (1) WOCE/TOGA drifters have a drogue at 15-m depth, whereas the model drifter is the upper layer average velocity; i.e., its effective drogue depth is nominally 40 m, but it is 50 m or greater in some locations. Therefore, the WOCE drifters are more influenced by Ekman currents. (2) Errors in the wind forcing may produce small latitudinal shifts in the zonal equatorial currents. If a drifter is seeded near the boundary between two counter-flowing currents, e.g., SEC and NECC, and the model-simulated current is displaced northward or southward, large buoy separation errors may result (Fig. 6a). (3) Regions dominated by flow instabilities will also produce poor agreement between the observed and model drifters. This is especially true in the Kuroshio Extension region (Fig. 6b), but also applies to the PWC region as well as equatorial latitudes (Fig. 4 c,e). The 1/4° horizontal resolution is only marginally eddy-resolving and many eddies in the PWC and equatorial regions are a smaller scale than can be resolved.

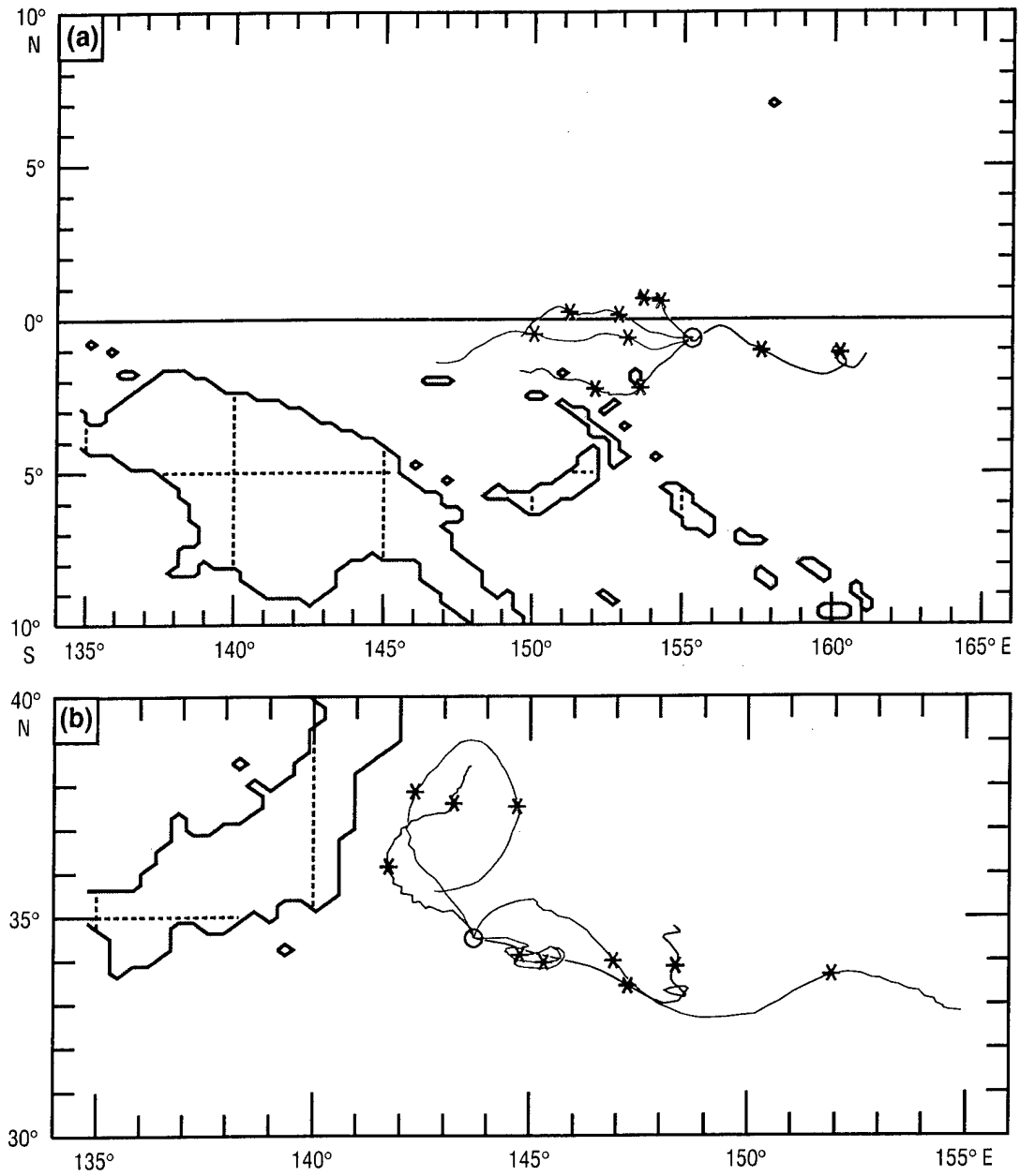

Fig. 6 — A 30-d segment of the four model-simulated buoys (color) and WOCE/TOGA (black): (a) drifting buoy 5909 in the equatorial Pacific and (b) drifting buoy 525 in the Kuroshio Extension region. The circle indicates the start location and the stars indicate 10-d increments from the initial deployment time.

Figure 7 shows three typical WOCE/TOGA drifter tracks; two are in the equatorial Pacific and the third is in the PWC region. Each traverses a very circuitous pathway over the buoy lifespan and appears to be caught in mesoscale eddies at one point or another. Figure 8 focuses in on a 30-d segment of each track and shows the WOCE drifter along with the four model-simulated drifters. When a drifter enters a zonal flow regime (Fig. 8a), the model can accurately track the observed drifter. However, this is more of the exception than the rule. In general, the equatorial velocity components are nondeterministic; simulated drifters not only differ from the observed data, but they also differ between each realization. Figure 8b highlights the nondeterminism of the SEC bifurcation

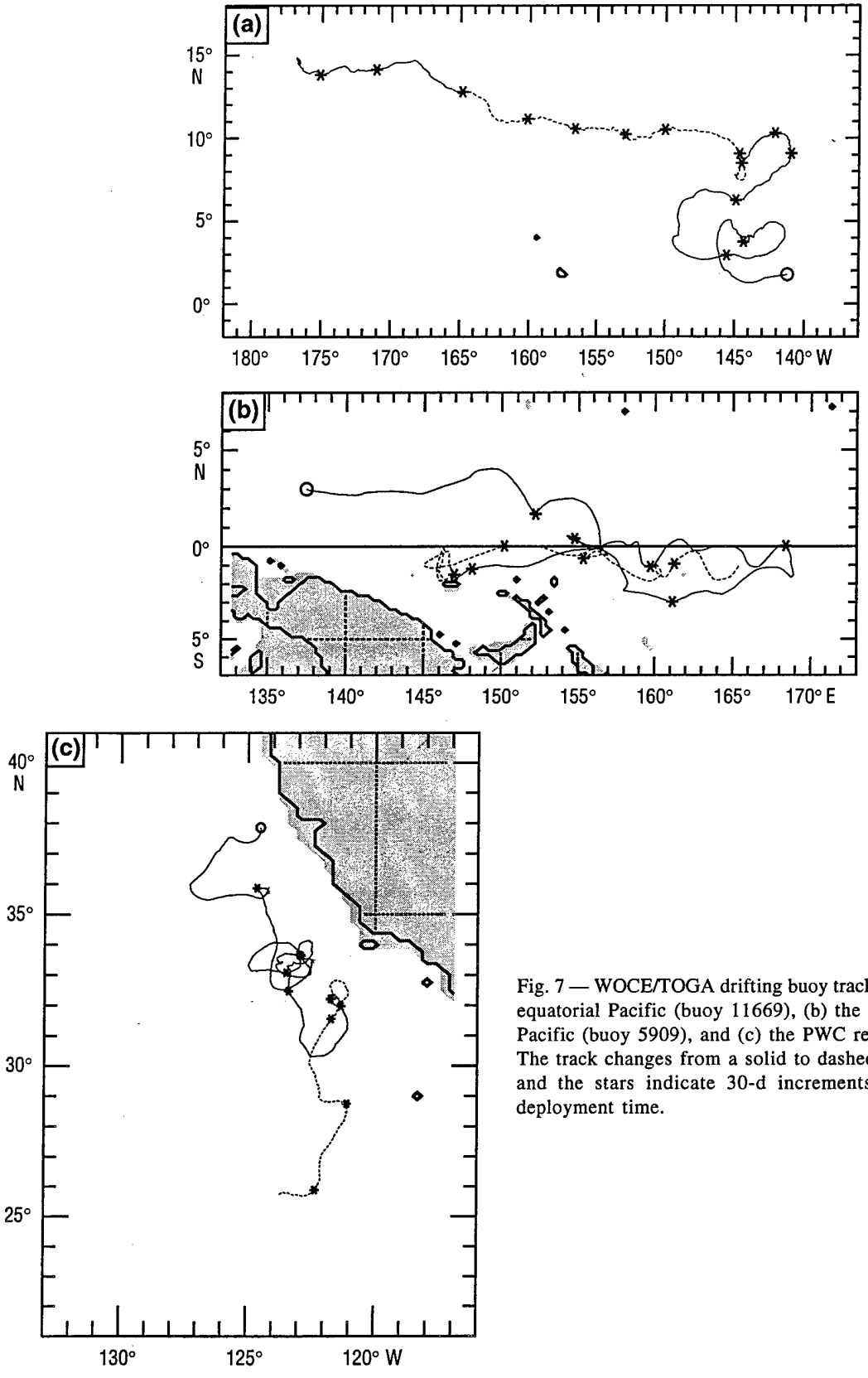

Fig. 7 — WOCE/TOGA drifting buoy tracks in (a) the eastern equatorial Pacific (buoy 11669), (b) the western equatorial Pacific (buoy 5909), and (c) the PWC region (buoy 7509). The track changes from a solid to dashed line every 183 d and the stars indicate 30-d increments from the initial deployment time.

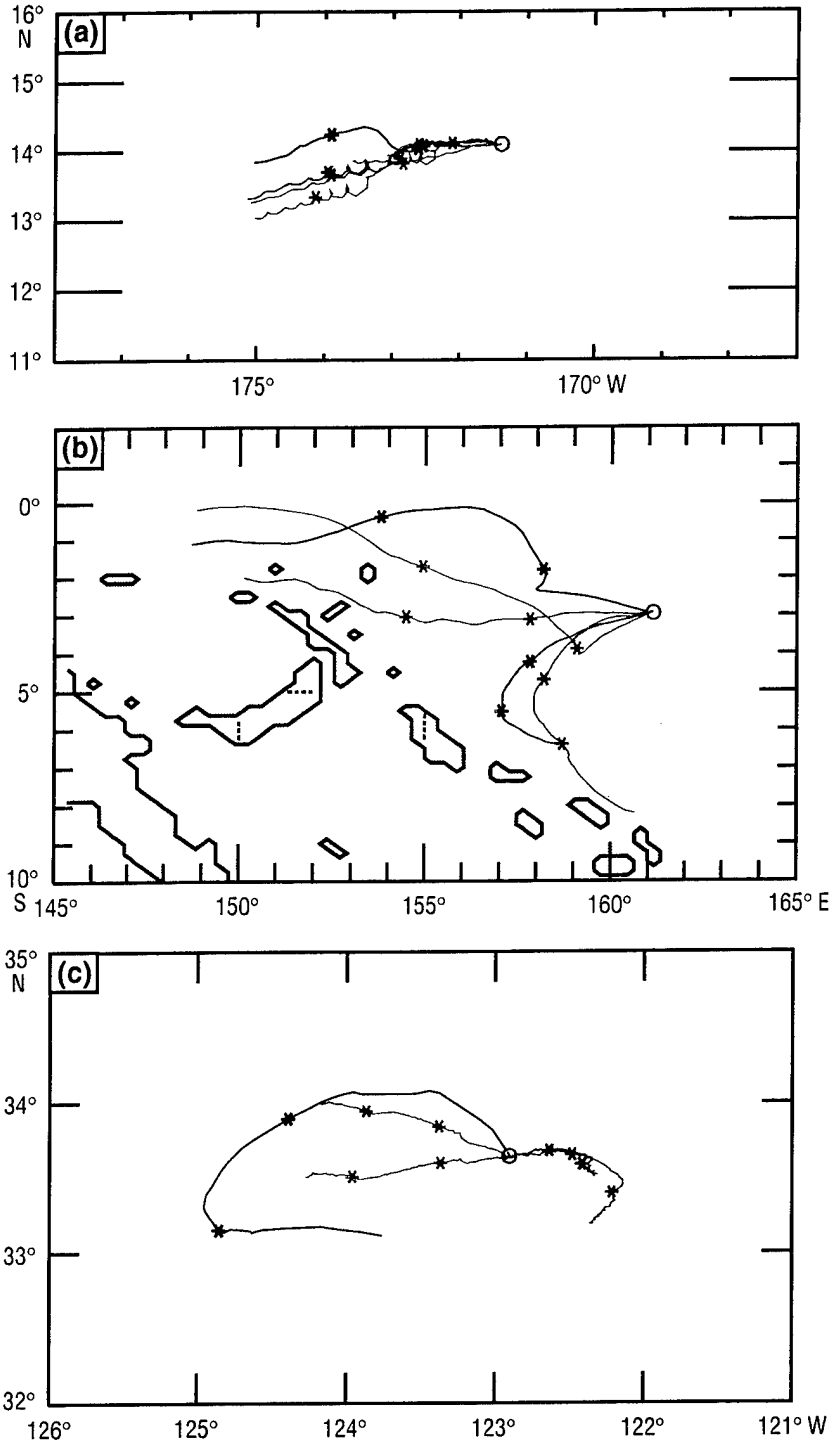

Fig. 8 — As in Fig. 6, except (a) buoy 11669, (b) buoy 5909, and (c) buoy 7509

east of the Solomon Seas and Fig. 8c shows a WOCE drifter caught in an eddy field off the California coast.

Drifting buoy separation distance versus time is shown in Fig. 9. The curves are the average separation distance between the observed drifter and an average of the four simulated buoys for all the redeploys of an individual buoy track. The simulated model drifters beat persistence in the eastern Pacific (Fig. 9a), but are the same as persistence for the other two buoys shown. Subjective analysis of all 19 buoy separation plots indicate the model was better than persistence in six cases, persistence beat the model in one case, and the model and persistence were comparable in 12 cases. These results are not surprising given the amount of nondeterminism of the upper-ocean velocity field.

3.5 Value Added of NLOM to the PWC Model

The IGOSS sea level data for the four U.S. west coast stations have also been compared against three simulations of the PWC model. All PWC experiments were forced 1992–1996 with the 12-hourly FNMOC NOGAPS/HR hybrid winds. NLOM supplied the boundary conditions and for experiment PWC17, NLOM was forced with these same FNMOC/HR winds. For experiment PWC14, NLOM was forced with climatological HR monthly winds and in experiment PWC19, no boundary conditions

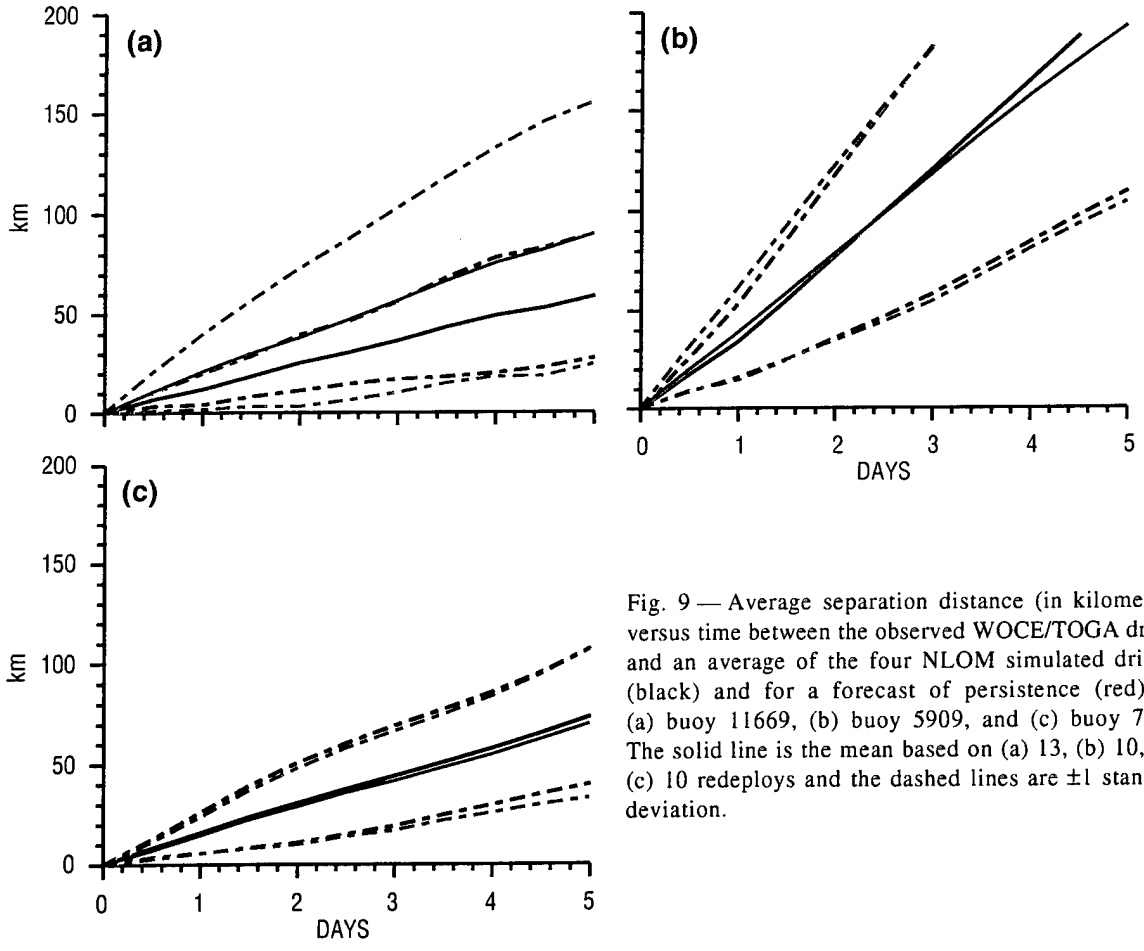

Fig. 9 — Average separation distance (in kilometers) versus time between the observed WOCE/TOGA drifter and an average of the four NLOM simulated drifters (black) and for a forecast of persistence (red) for (a) buoy 11669, (b) buoy 5909, and (c) buoy 7509. The solid line is the mean based on (a) 13, (b) 10, and (c) 10 redeploys and the dashed lines are ±1 standard deviation.

Table 4 — Correlation Coefficients Between Observed IGOSS Sea Level Data and the PWC Model. PWC was Forced 1992–1996 with the 12-Hourly FNMOC NOGAPS/HR Hybrid Winds. NLOM Provided Boundary Conditions to PWC and was Forced with the Same 12-Hourly FNMOC NOGAPS/HR Hybrid Winds (PWC17) or Climatological HR Monthly Mean Winds (PWC14). In PWC19, No Boundary Conditions from NLOM were Used. Correlations are Computed for Both the Monthly and Daily Data and the First 3 mo. of the Time Series are Excluded. The Daily Output has a 1-2-1 Filter Applied.

IGOSS STATION	LOCATION	PWC17	PWC14	PWC19
Monthly				
Neah Bay, WA	48°22′ N, 124°34′ W	0.94	0.92	0.78
Crescent City, CA	41°45′ N, 124°12′ W	0.87	0.75	0.67
San Francisco, CA	37°48′ N, 122°28′ W	0.78	0.66	0.46
San Diego, CA	32°42′ N, 117°10′ W	0.60	–0.36	0.08
Daily				
Neah Bay, WA	48°22′ N, 124°34′ W	0.88	0.85	0.77
Crescent City, CA	41°45′ N, 124°12′ W	0.83	0.75	0.68
San Francisco, CA	37°48′ N, 122°28′ W	0.75	0.65	0.56
San Diego, CA	32°42′ N, 117°10′ W	0.54	–0.27	0.08

from NLOM were used. Table 4 lists the IGOSS versus PWC correlations and Fig. 10 shows the daily IGOSS versus experiment PWC17 sea level curves.

The main reason for coupling PWC to NLOM is to provide boundary conditions and, thus, transmit oceanic information outside the PWC region into that domain. Table 4 indicates a positive effect when using NLOM boundary conditions that had the same wind forcing. At all stations, PWC17 correlations are higher than PWC14 correlations (climatological NLOM forcing) and both are clearly higher than using no boundary conditions from NLOM (PWC19). The effect is most dramatic at San Diego. The improvement in correlation is most likely due to the fact that coastally trapped Kelvin waves propagate northward along the U.S. west coast and the seasonal sea level variability can be affected by these waves. It is unknown as to why this effect diminishes poleward, but increasing correlation from south to north for these four stations is a common feature in many of the NLOM simulations forced with interannual winds. Jacobs et al. (1994) discusses this Kelvin/Rossby wave generation along the west coast and has related large interannual events to the El Niño/Southern Oscillation (ENSO).

The non-optimal approach of implementing PWC boundary conditions from NLOM may also contribute to only modest improvements at the northern three stations in Table 4. The coupling scheme should incorporate the vertical structure, but the missing piece of this first-generation scheme is the baroclinic component that will capture the internal Kelvin and Rossby wave signals. How can the vertical profile be obtained? Several options exist. (1) Use SSH from NLOM and apply the synthetic technique of Carnes et al. (1996) as discussed in Sec. 2.2. (2) The density profile from NLOM should be relatively accurate and it could be interpolated in the vertical. Absolute density or deviations from a long-term mean could then be used to calculate temperature

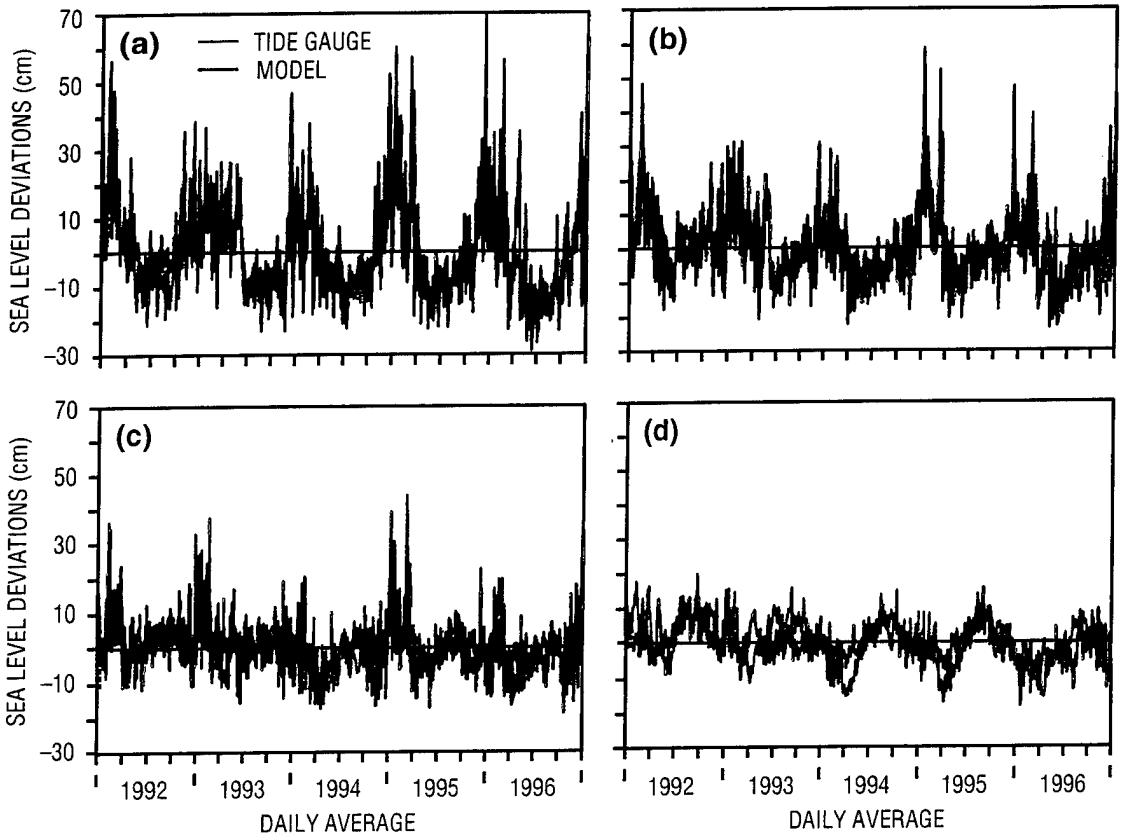

Fig. 10 — Observed daily IGOSS versus experiment PWC17 simulated sea level for four stations along the U.S. west coast: (a) Neah Bay, WA, (b) Crescent City, CA, (c) San Francisco, CA, and (d) San Diego, CA. The correlation coefficients are 0.86, 0.81, 0.67, and 0.49, respectively. IGOSS data are the red curves and the model data are blue. The data have a 1-2-1 running filter applied to remove some of the tidal effects.

and salinity. (3) The statistical inference techniques from Hurlburt et al. (1990) could be applied in PWC to project surface information downward.

While the sea level variability along the U.S. west coast appears to be largely driven by seasonal winds, the results of Table 4 can be misleading because of the time frame over which the correlations are computed. There are no large, coastally trapped Kelvin wave events between 1992 and 1995, and hence, climatological boundary conditions appear to be adequate. But analysis from two 1/8° Pacific basin models run 1981–1995 with the 12-hourly ECMWF/HR hybrid winds suggests even small tropically generated Kelvin waves propagating into the PWC region can greatly impact sea level correlations. The two 1/8° models only differ in that one has a southern boundary at 20° S (p133) and the other is at 14° N (p333) and excludes the equatorial latitudes. The 1992–1995 monthly sea level correlations for these two simulations are seen in Table 5. The exclusion of the tropical latitudes has significantly reduced the sea level correlations, especially for the southern three stations. The coastally trapped Kelvin waves generated in the tropics appear to be a large part of the sea level signal and the effect is greater equatorward. This example highlights the need for the basin-scale NLOM providing boundary conditions for the regional PWC model.

Table 5 — The 1992–1995 Correlation Coefficients Between Observed IGOSS Sea Level Data and Two 1/8° Pacific Ocean NLOM Simulations Forced by ECMWF/HR Hybrid Winds. Model p133 has a Southern Boundary at 20° S and Model p333 has a Southern Boundary at 14° N. The IGOSS Data are Monthly Averages and a 30-d Running Mean Filter has been Applied to the Model Results.

IGOSS STATION	LOCATION	p133	p333
Monthly			
Neah Bay, WA	48°22′ N, 124°34′ W	0.92	0.86
Crescent City, CA	41°45′ N, 124°12′ W	0.92	0.65
San Francisco, CA	37°48′ N, 122°28′ W	0.86	0.47
San Diego, CA	32°42′ N, 117°10′ W	0.62	0.42

4.0 SUMMARY, CONCLUSIONS, AND RECOMMENDATIONS

The components of OCEANS 1.0 have been described in this report. They consist of the 1/4° global, **reduced gravity** thermodynamic NLOM and PWC models. NLOM is marginally eddy-resolving at 1/4° resolution and, in general, it can accurately depict the large-scale circulation of the world oceans. Two major exceptions are the Gulf Stream and Agulhas Retroflection; the former requires much higher horizontal resolution and the latter requires upper ocean – topographic coupling, which is absent in the reduced gravity model. A 1/4° **finite depth** version of the model, now running in real time at FNMOC, has greatly improved the model results in the Agulhas Retroflection region and has marginally improved the simulation of the Kuroshio and Gulf Stream due to the inclusion of the bottom topography, improved physics, and altimeter data assimilation.

The reduced gravity version of NLOM validated here is wind-forced only with no assimilation of altimeter or IR frontal data. Thus, it cannot be expected to produce accurate hindcasts of SSH or upper-ocean velocities in regions dominated by mesoscale (or smaller) flow instabilities. Maps have been provided to show the relative importance of direct wind forcing (deterministic) versus flow instabilities (nondeterministic). These must be taken into account when judging the performance of NLOM.

NLOM has mixed success in hindcasting sea level variations when compared to observed tide gauges. However, some of the highest correlations are at stations within the PWC domain. Ultimately, the impact of satellite altimetry assimilation will be the most substantial where the skill of the wind-driven model is relatively low and the space-time scales of the SSH variations are resolved by the altimeter.

A comparison between observed and NLOM simulated drifting buoys has also been made. A number of factors have been defined indicating possible sources of error, and thus, the model has only partial success in tracking observed drifting buoys. An ensemble forecast of four model simulations (each of which start from a different initial state) generally produces an average simulated track that is closer to the observed drifter than any one single simulation. However, the model cannot consistently beat a persistence forecast due to the large amount of nondeterminism in the

upper layer velocity fields. But a set of multiple drifter tracks could be beneficial in SAR applications as the endpoint envelope could define a search area. A tight packing would indicate higher confidence in the model forecast whereas a widespread distribution would indicate the presence of flow instabilities and lower model confidence.

NLOM will also provide boundary conditions for the PWC model. Sea level comparisons were also made between observed data and two PWC simulations, one that used climatologically wind-forced NLOM boundary conditions and one that used interannually wind-forced NLOM boundary conditions. The case that used interannually forced NLOM boundary conditions showed modest improvement in sea level correlation for one of the west coast stations, substantial improvement for two, and dramatic improvement at the southernmost station. Satellite altimetry assimilation and an improvement in the boundary condition coupling scheme will more than likely improve this situation. In particular, the inclusion of the baroclinic component from NLOM should improve the transfer of information into PWC. The improvement when using interannual NLOM boundary conditions in the PWC can also be somewhat misleading because of the time frame used. The sea level signal at these stations can be affected by coastally trapped Kelvin waves that propagate poleward after being equatorially generated. ENSO events have been shown to generate such waves. The 1992–1995 time period did not have any large ENSO events, so climatologically wind-forced NLOM boundary conditions appear to be adequate. However, NLOM simulations that exclude the equatorial latitudes show a substantial reduction in sea level correlation along the west coast, thus highlighting the need for boundary conditions from a larger scale model.

Due to the limitations in physics of the 1/4° **reduced gravity** NLOM and the lack of satellite data assimilation, it is recommended that OCEANS 1.0 not enter operational check/test mode. Because a 1/4° thermodynamic **finite depth** version of the NLOM with assimilation of TOPEX/Poseidon and ERS-2 altimeter data is now running in real time at FNMOC, it is recommended this model version be used. Additionally, further refinement of the boundary condition coupling scheme may improve the transfer of information from the global model to the regional model. Thus, the schedule for OCEANS 1.1 should be accelerated given the potential for improvement.

To date, the validation work on the NLOM has been minimal due to a low level of funding. Much more can and should be done, although funding may again be an issue. The atmospheric centers have been using an ensemble prediction system that has the capability of estimating the skill of a deterministic forecast (Biuzza 1997). Such a system should be considered within operational testing, although computational resources may be a limiting factor.

5.0 ACKNOWLEDGMENTS

This work was performed as part of the Naval Research Laboratory 6.4 Large-Scale Models project, managed by the Space and Naval Warfare Systems Command under program element 0603207N. It is also a contribution to the 6.2 Global Ocean Prediction System project, modeling task at NRL, as part of the Naval Ocean Modeling and Prediction program under program element 0602435N at the Office of Naval Research. The numerical simulations were performed on the Cray T3D MC128 at the Arctic Region Supercomputing Center, University of Alaska, Fairbanks, AK, the Thinking Machines CM5 at the Naval Research Laboratory, Washington, D.C., and the Silicon Graphics Power Challenge Array at the Naval Oceanographic Office, Stennis Space Center, MS. All are part of the Defense Department's High Performance Computing Initiative.

6.0 REFERENCES

Batteen, M. L., C. A. Collins, C. R. Gunderson, and C. S. Nelson, "The Effect of Salinity on Density in the California Current System," *J. Geophys. Res.* **100**, 8733–8749 (1995).

Biuzza, R., "Potential Forecast Skill of Ensemble Prediction and Spread and Skill Distribution of the ECMWF Ensemble Prediction System," *Mon. Weather Rev.* **125**, 99–119 (1997).

Blumberg, A. F. and G. L. Mellor, "A Description of a Three-Dimensional Coastal Ocean Circulation Model," in *Three-Dimensional Coastal Ocean Models, Vol. 4*, N. Heaps (ed.), (American Geophysical Union, Washington, D.C., 1987), p. 208.

Carnes, M. R., D. N. Fox, R. C. Rhodes, and O. M. Smedstad, "Data Assimilation in a North Pacific Ocean Monitoring and Prediction System," in *Modern Approaches to Data Assimilation in Ocean Modeling*, Elsevier Oceanography Series 61, P. Malanotte-Rizzoli (ed.), (Elsevier Publishing Co., 1996), p. 455.

Flather, R. A., "A Tidal Model of the Northwest European Continental Shelf," *Mern. Soc. R. Sci. Lieye,* Ser. 6, **10**, 141–164 (1976).

Fratantoni, D. M., W. E. Johns, and T. L. Townsend, "Rings of the North Brazil Current: Their Structure and Behavior Inferred from Observations and a Numerical Simulation," *J. Geophys. Res.* **100**, 10,633–10,654 (1995).

Gouriou, Y. and G. Reverdin, "Isopycnal and Diapycnal Circulation of the Upper Equatorial Atlantic Ocean in 1983–1984," *J. Geophys. Res.* **97**, 3543–3572 (1992).

Hellerman, S. and M. Rosenstein, "Normal Monthly Wind Stress Over the World Ocean with Error Estimates," *J. Phys. Oceanog.* **13**, 1093–1104 (1983).

Hurlburt, H. E. and P. J. Hogan, "Dependence of Gulf Stream Simulations on Grid Resolution, 1/2° to 1/32°," *abstract from Data Assimilation and Model Evaluation Experiments–North Atlantic Basin (DAMEE-NAB) Information Exchange Meeting #4,* http://www.coam.usm.edu/damee/iem4.html, Institute of Marine Sciences, University of Southern Mississippi, Stennis Space Center, MS, 24–26 Mar (1997).

Hurlburt, H. E. and J. D. Thompson, "A Numerical Study of Loop Current Intrusions and Eddy Shedding," *J. Phys. Oceanog.* **10**, 1611–1651 (1980).

Hurlburt, H. E., M. R. Carnes, D. N. Fox, E. J. Metzger, O. M. Smedstad, and A. J. Wallcraft, "Eddy-Resolving Ocean Modeling and Prediction in the Pacific Ocean with Assimilation of Satellite Altimeter and IR Data," *Actes du Colloque Oceanogaphie Operationnelle et Observation Spatiale*, Biarritz, France; Meteo, France, CNES, SMF, pp. 105–119 (1996a).

Hurlburt, H. E., D. N. Fox, and E. J. Metzger, "Statistical Inference of Weakly Correlated Subthermocline Fields from Satellite Altimeter Data," *J. Geophys. Res.* **95**, 11,375–11,409 (1990).

Hurlburt, H. E., A. J. Wallcraft, W. J. Schmitz, Jr., P. J. Hogan, and E. J. Metzger, "Dynamics of the Kuroshio/Oyashio Current System Using Eddy-Resolving Models of the North Pacific Ocean," *J. Geophys. Res.* **101**, 941–976 (1996b).

Jacobs, G. A., H. E. Hurlburt, J. C. Kindle, E. J. Metzger, J. L. Mitchell, W. J. Teague, and A. J. Wallcraft, "Decadal-Scale Trans-Pacific Propagation and Warming Effects of an El Niño Anomaly," *Nature* **370**, 360–363 (1994).

Larson, J. C., "Transport and Heat Flux of the Florida Current at 27° N Derived from Cross-Stream Voltages and Profiling Data: Theory and Observations," *Philosophical Transactions of the Royal Society of London* **338**, 169–236 (1992).

Levitus, S., "Climatological Atlas of the World Ocean," *NOAA Professional Paper 13* (Geophysical Fluid Dynamics Laboratory, Princeton, NJ, 1982), 173 pp.

Lukas, R. and E. Firing, "The Geostrophic Balance of the Pacific Equatorial Undercurrent," *Deep-Sea Research,* **31**, 61–66 (1984).

Lukas, R., E. Firing, P. Hacker, P. Richardson, C. Collins, R. Fine, and R. Gammon, "Observations of the Mindanao Current During the Western Equatorial Pacific Ocean Circulation Study," *J. Geophys. Res.* **96**, 7089–7104 (1991).

Lukas, R., T. Yamagata, and J. P. McCreary, "Pacific Low-Latitude Western Boundary Currents and the Indonesian Throughflow," *J. Geophys. Res.* **101**, 12,209–12,216 (1996).

Metzger, E. J. and H. E. Hurlburt, "Coupled Dynamics of the South China Sea, the Sulu Sea, and the Pacific Ocean," *J. Geophys. Res.* **101**, 12,331–12,352 (1996).

Metzger, E. J., H. E. Hurlburt, J. C. Kindle, Z. Sirkes, and J. M. Pringle, "Hindcasting of Wind-Driven Anomalies Using a Reduced-Gravity Global Ocean Model," *Mar. Technol. Soc. J.* **26**(2), 23–32 (1992).

Metzger, E. J., H. E. Hurlburt, G. A. Jacobs, and J. C. Kindle, "Hindcasting of Wind-Driven Anomalies Using Reduced-Gravity Global Ocean Models with 1/2° and 1/4° Resolution," NRL/FR/7323--93-9444, Naval Research Laboratory, Stennis Space Center, MS, 1994.

Moore, D. R. and A. J. Wallcraft, "Formulation of the Navy Layered Ocean Model in Spherical Coordinates," NRL/CR/7323--96-0005, Naval Research Laboratory, Stennis Space Center, MS, 1996.

Munk, W. H., "On the Wind Driven Ocean Circulation," *J. Meteorol.* **7**, 79–93 (1950).

Nowlin, W. D., "Winter Circulation Patterns and Property Distributions," in *Contributions on the Physical Oceanography of the Gulf of Mexico,* Vol. II, L. R. A. Capurro and J. L. Reid (eds.), (Gulf Publishing Co., 1972), p. 3–51.

Philander, S. G., "El Niño, La Niña, and the Southern Oscillation," *International Geophysics Series, Vol. 46,* R. Dmowska and J. R. Holton (eds.), (Academic Press, Inc., San Diego, CA, 1990), 293 pp.

Shriver, J. F. and H. E. Hurlburt, "The Contribution of the Global Thermohaline Circulation to the Pacific to Indian Ocean Throughflow via Indonesia," *J. Geophys. Res.* **102**, 5491–5511 (1997).

Smedstad, O. M., D. N. Fox, H. E. Hurlburt, G. A. Jacobs, E. J. Metzger, and J. L. Mitchell, "Altimeter Data Assimilation into a 1/8° Eddy Resolving Model of the Pacific Ocean,"*J. of the Meteorological Soc. of Japan* **75**(1B), 429–444 (1997).

Sverdrup, H. E., "Wind-Driven Currents in a Baroclinic Ocean: With Application to the Equatorial Currents of the Eastern Pacific," *Biogr. Mem. Natl. Acad. Sci. U.S.A.* **33**, 318–326 (1947).

Teague, W. J., M. J. Carron, and P. J. Hogan, "A Comparison Between the Generalized Digital Environmental Model and Levitus Climatologies," *J. Geophys. Res.* **95**, 7167–7183 (1990).

Teague, W. J. and P. J. Hogan, "Regional Plots from the GDEM and Levitus Climatologies," NORDA Tech. Note 361, Naval Research Laboratory, Stennis Space Center, MS (1989).

Toole, J. M., R. C. Millard, Z. Wang, and S. Pu, "Observations of the Pacific North Equatorial Current Bifurcation at the Philippine Coast," *J. Phys. Oceanog.* **20**, 307–318 (1990).

Wyrtki, K. and B. Kilonsky, "Mean Water and Current Structure During the Hawaii-to-Tahiti Shuttle Experiment," *J. Phys. Oceanog.* **14**, 242–254 (1984).

Wallcraft, A. J., "The Navy Layered Ocean Model Users Guide," NOARL Report 35, Naval Research Laboratory, Stennis Space Center, MS, 1991.

Wallcraft, A. J. and D. R. Moore, "A Scalable Implementation of the Navy Layered Ocean Model," NRL/CR/7323--96-0006, Naval Research Laboratory, Stennis Space Center, MS, 1996.